International Journal of Nanomedicine

Dovepress
open access to scientific and medical research

Open Access Full Text Article

ORIGINAL RESEARCH

Dual-Target Multifunctional Superparamagnetic Cationic Nanoliposomes for Multimodal Imaging-Guided Synergistic Photothermal/ Photodynamic Therapy of Retinoblastoma

Wendi Zheng[1,2,*], Xing Li[1,2,*], Hongmi Zou[1,2], Yan Xu[1], Pan Li[2], Xiyuan Zhou[1], Mingxing Wu[1]

[1]Department of Ophthalmology, the Second Affiliated Hospital of Chongqing Medical University, Chongqing, People's Republic of China; [2]Chongqing Key Laboratory of Ultrasound Molecular Imaging, Institute of Ultrasound Imaging of Chongqing Medical University, Chongqing, People's Republic of China

*These authors contributed equally to this work

Correspondence: Mingxing Wu; Xiyuan Zhou, Department of Ophthalmology, the Second Affiliated Hospital of Chongqing Medical University, 74 Linjiang Road, Yuzhong District, Chongqing, People's Republic of China, Tel +86 183 2342 5867; +86 139 9628 6679, Email 304873@hospital.cqmu.edu.cn; zhouxiyuan2002@aliyun.com

Background: With high malignancy, retinoblastoma (RB) commonly occurs in infants and has incredible difficulty with the early diagnosis. In recent years, the integrated theranostics of multimodal imaging-guided therapy has shown promising potential for oncotherapy.

Purpose: To prepare folate/magnetic dual-target theranostic nanoparticles integrating with US/PA/MR imaging and the synergistic photothermal treatment (PTT)/photodynamic treatment (PDT) for the early diagnosis and timely intervention of RB cancer.

Methods: Folate/magnetic dual-target cationic nanoliposomes (CN) encapsulating indocyanine green (ICG) and perfluorohexane-(PFH)(FA-CN-PFH-ICG-Fe_3O_4, FCNPIFE) were synthesized and characterized. Then we evaluated their targeting ability, US/PA/MR imaging effects, and the efficacy of synergistic PTT/PDT in vitro and in vivo. Finally, we explored the mechanism of synergistic PTT/PDT in Y79 tumor-bearing mice.

Results: FCNPIFEs were stable and uniform in 7 days. They showed excellent in vitro targeting ability with a 95.29% cell uptake rate. The in vitro US/PA/MRI imaging results of FCNPIFEs showed a concentration-dependent manner, and in vitro therapy FCNPIFEs exhibited an enhanced anticancer efficacy against Y79 cells. In vivo analysis confirmed that FCNPIFEs enabled a targeted synergistic PTT/PDT under US/PA/MR imaging guidance in Y79 tumor-bearing mice, achieving almost complete tumor regression. Immunofluorescence results displayed weaker fluorescence intensity compared with other single treatment groups, confirming that PTT/PDT synergistic therapy effect was achieved by down-regulating the expression of HIF-1α and HSP70.

Conclusion: FCNPIFEs were verified as promising theranostic nanoliposomes for RB oncotherapy and showed great potential in clinical application.

Keywords: nanomedicine, retinoblastoma, theranostic, phototherapy

Introduction

Retinoblastoma (RB) is an intraocular malignant tumor commonly found in infants.[1] The patients' mortality rate and visual preservation degree depend on the disease progression at the first visit.[2,3] Due to insufficient public understanding of RB, the diagnosis and treatment of RB in developing countries are often delayed, which leads to excessive tumor growth, or even worse, extra-ocular metastases.[4] Under such circumstances, children fail to retain their vision and face serious life threats with a mortality rate up to 70%.[5] Therefore, early diagnosis based on clear imaging evidence and timely medical intervention are the priorities in RB management.

Received: 27 February 2022
Accepted: 16 July 2022
Published: 26 July 2022

International Journal of Nanomedicine 2022:17 3217–3237

By integrating diagnosis and treatment, theranostics provide more precise therapeutic schemes and endure popularity in anticancer research for long time.[6] In recent years, the flexible and diverse nanostructures derived from nanotechnology have sparked new ideas for cancer therapy by merging diagnostic and therapeutic functions into one single nanoplatform.[7,8] Thus, it is an attractive idea to design a unique nanoplatform to treat RB safely and effectively under the guidance of appropriate imaging techniques.

Enucleation surgery, radiotherapy, chemotherapy, and gene therapy constitute the central therapeutic axis to suppress RB progression. Nevertheless, enucleation is the most destructive treatment in ophthalmology, whereas the three other therapies can cause high tumor recurrence rates, treatment resistance, or severe ocular toxicity.[3] Therefore, local non-invasive therapeutic strategies may be more suitable alternatives to treat RB cancer safely. Phototherapy,[9] particularly photothermal therapy (PTT) and photodynamic therapy (PDT), is widely used as an anticancer strategy due to its non-invasion, poor side effect, and good spatiotemporal controllability. In many research,[10,11] PTT, PDT, and multimodal imaging technologies were successfully integrated into a single nanoplatform and displayed excellent antitumor efficiency. The application of such nanoplatforms in ocular tumors is still blank and it will show bright prospects in the treatment of RB. However, considering the specific anatomy structure of the eyeball, these existing nanoplatforms need to be further optimized before they are used for RB therapy.

Photothermal agents used in photothermal therapy (PTT) can transform light energy into heat energy, which results in thermal ablation to tumor tissues.[12–14] Otherwise, PTT monotherapy is easy for inducing an overexpressed level of heat shock protein (HSP) in tumor cells, leading to an apparent reduction of therapeutic efficacy.[15,16] Photosensitizers used in PDT can generate reactive oxygen species (ROS) under appropriate laser excitation, resulting in the apoptosis/necrocytosis of tumor cells without obvious toxicity to normal tissues.[17] Moreover, previous studies confirmed that PDT showed a more significant curative effect for the RB cell lines with strong resistance to chemotherapy and gene therapy.[18] However, the high dependence of photodynamic therapy on oxygen seriously restricts its efficacy. The two phototherapy techniques showed inherent limitations when applied separately, while many studies demonstrated that unifying PDT and PTT into one single nanoplatform could mutually repair the deficiency of the two techniques and show a synergistic antitumor effect.[19,20]

Nevertheless, in those studies, either two materials are required to act as photosensitizers and photothermal agents respectively,[21] or two light sources with different wavelengths are required as excitation conditions,[22] both of which increase the difficulty of clinical application. Therefore, finding an appropriate material that achieves both photodynamic and photothermal effects under a single excitation condition can significantly simplify the manufacturing process of nanoplatforms and thus avoid restrictions on clinical application. With low afford and high biosafety, ICG has often been used in fundus choroidal angiography[23] and commonly acted as a good photoacoustic imaging agent in many studies.[24,25] In addition to imageology functions, it is noteworthy that ICG also has excellent photothermal/photodynamic properties under the same excitation laser.[26] Given the limited photodynamic effects of ICG caused by hypoxia in the tumor microenvironment, PFH is considered an excellent option to remedy the deficiency. PFH is one kind of fluorocarbon, which can transform from liquid to gaseous state under the condition of photophase change (ODV)[27] and simultaneously release the pre-stored oxygen due to the oxygen-carrying function of PFH.[28] Except the reinforced PDT effects, PFH is able to enhance the ultrasonic imaging effect by microbubbles generated from the phase transition process.[29,30] Therefore, nanoparticles with PFH-ICG as the core can be regarded as ideal candidates to construct ocular multifunctional molecular probes for RB.

Nevertheless, designing theranostics nanoplatforms that balance and maximize the efficiency of features discussed above remains a challenge. The theranostics liposomes loaded with perfluorooctyl bromide (PFOB) and ICG have been constructed in related research by D. Sheng et al.[31] However, the uncomprehensive imaging techniques for early diagnosis of retinoblastoma and the poor targeting performance require the replacement of more suitable materials and further optimization for the adequate accumulation of nanoparticles in tumor regions. MRI, not PFOB-based CT, is the most recommended imaging monitoring method for RB patients retaining eyeball because it can identify early metastatic lesions and nearby tissue infiltration.[32] With Fe_3O_4 as the core, SPIONs can enhance T2 imaging signals and are widely chosen as an ideal MRI negative contrast agent.[33] Thus, more comprehensive, accurate, and real-time imaging evidence for RB can be provided by combining SPION-based MR imaging with ICG-based photoacoustic imaging and PFH-enhanced ultrasound imaging. Besides the MRI functions, SPIONs exhibited high targeted aggregation capability under the external magnetic field. The high targeted ability of SPIONs is not

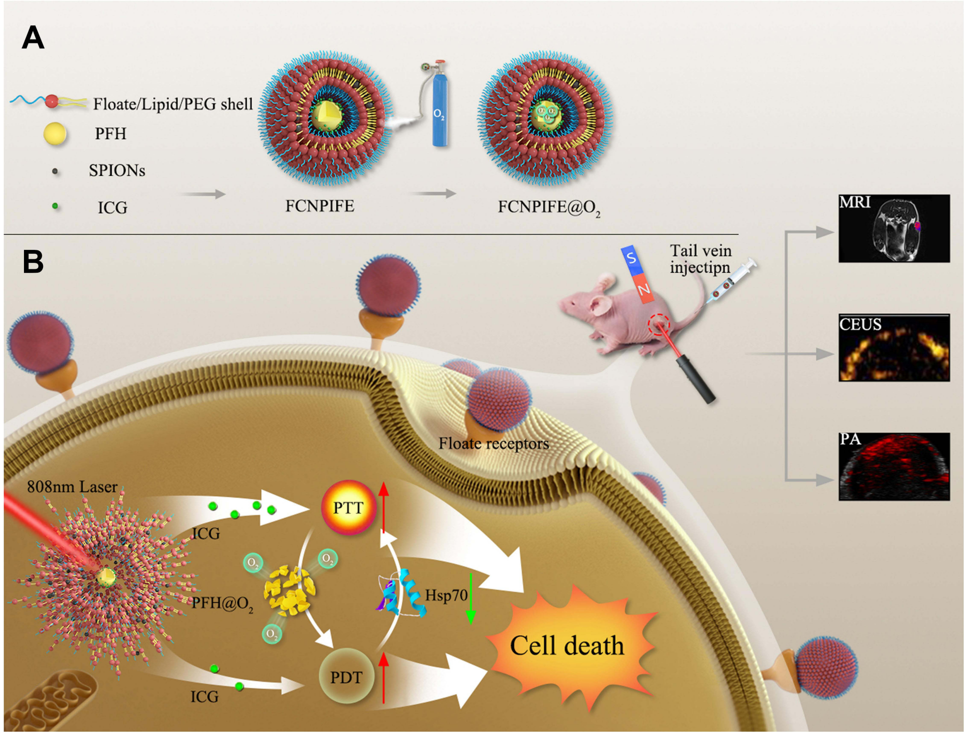

Scheme 1 Schematic illustration of (A) the synthesis of FCNPIFEs; (B) the synergistic photothermal/photodynamic therapy of retinoblastoma under the US/PA/MR imaging-guide.

affected by the differences in receptor expression among individuals and the receptor–antibody specific binding, showing advantages of high efficiency, stability, and low toxicity.[34] However, the magnetic target cannot improve the active uptake of nanoparticles by the tumor cells. Folate[35] and cationic cholesterol can be considered as excellent targeting modification materials to compensate for the deficiency of the single magnetic target of Fe3O4 (folate/magnetic dual-target cationic nanoliposomes), on account of the overexpression of folate receptor by Y79 cells[36] and the electrostatic adsorption on the tumor cell surface by cationic liposomes.[37] The remodified nanoparticles can further promote the phagocytosis of Y79 cells.

In this work, Folate-CN-PFH-ICG-Fe_3O_4 (FCNPIFE) was constructed as shown in Scheme 1A. Under 808nm laser excitation, FCNPIFE could implement synergistic PTT/PDT treatment with the US/PA/MRI multimodal imaging-guided (Scheme 1B). The folate/magnetic dual-target and the electrostatic adsorption induced by cationic cholesterol facilitate accumulations of FCNPIFEs in tumor regions. Under the powerful oxygen delivery function of PFH, tumor hypoxia was greatly alleviated and PDT efficacy of ICG in hypoxia was paralleled to that in normoxia. Furthermore, the enhanced PDT effects would reduce the expression of heat shock protein (HSP)[38] and effectively improve tumor cells' sensitivity to photothermal effects of ICG. It is noticeable that ICG, PFH and SPIONs were multifunctional that ICG and PFH combined both treatment and imaging functions, as well as SPIONs combined imaging functions and targeting properties. The multifunctional components of FCNPIFE make the overall design of the nanoplatform extremely coordinated and greatly simplifies the synthesis process. It lowered manufacturing costs while guaranteed excellent anti-tumor efficiency, compared with our previous study that performed gene therapy[39] and immunotherapy[40] to RB cancer. The FCNPIFE nanoplatforms showed remarkable potential for early diagnosis of RB and timely intervention of RB tumors.

Materials and Methods

Materials and Reagents

DPPC (1,2-Dihexadecanoyl-rac-Glycero-3-Phosphocholine), DSPE-PEG (2000)-FA (1,2-distearoyl-sn-glyc-ero-3-phosphoethanolamine-N-[folate(polyethylene glycol)-2000]) and Superparamagnetic iron oxide nanoparticles (SPION, cored as Fe_3O_4) were gained from Xi'an ruixi biological technology (China). Indocyanine (ICG), perfluorohexane (PFH) and

Dc-cholesterol (3- (N- (N’, N’-Dimethylaminoethane) were obtained from Sigma Aldrich (St. Louis, MO, USA). Reactive Oxygen Species Assay Kit (2′,7′-dichlorofluorescin diacetate, DCFH-DA), 1,1′-dioctadecyl-3,3,3′,3′-tetramethylindocarbocyanine perchlorate (DiI), 3.3-dioctadecyloxacarbocyanine perchlorate (DiO) and 2-(4-Amidinophenyl)-6-indolecarbamidine dihydrochloride (DAPI) were gained from Beyotime Biotechnology (China). Calcein-AM (CAM) and 1.1′-dioctadecyl-3,3,3′,3′-tetramethylindotricarbocyanine iodide (DiR) were purchased from Santa Cruz Biotechnology (TX, USA). Roswell Park Memorial Institute-1640 (RPMI-1640) was acquired from Corning (New York, NY, USA). Fetal bovine serum (FBS) was obtained from Capricorn Scientific GmbH (Ebsdorfergrund, Germany). Cell counting kit-8 (CCK-8) assay was acquired from Dojindo Laboratories (Kumamoto, Japan). All chemicals were of analytical grade and used without further purification.

Synthesis of FCNPIFE Liposomes

For the dual-targeted FCNPIFE nanoplatforms, the preparation contained film dispersion method and two-step emulsion method as described previously.[31] The mixture of 5.5 mg DPPC, 2.5 mg DSPE-PEG2000-FA, 2.5 mg DC-Chol and 25uL SPIONs (10 mg/mL) were fully dissolved in 5 mL trichloromethane, and the solution was evaporated by rotary evaporator (50°C) for 2h to form brown lipid film with addition of hydration 2 mL of PBS to hydrate the lipid films for later use. Next, the mixture of 2 mg ICG hydration and 0.2 mL of PFH was sonicated in ice bath for 2 min with 35% power (on 5 s; off 5 s) by sonicator (Heat System Inc, USA) as the first-step emulsion. Then the brown lipid films were added to the ICG-PFH solution and had emulsified for another 6 min with 40% power (on 5 s; off 5 s). Finally, the FCNPIFEs were centrifuged for three times (8000 rpm, 5 min) to obtain purified nanoliposomes and stored at 4°C for further use. The difference in FNNPIFEs (Folate-NN-PFH-ICG-Fe_3O_4, FNNPIFE) is that normal cholesterol, not Dc-cholesterol, was used for preparation in contrast to FCNPIFEs. The preparation of FCNPI (Folate-CN-PFH-ICG, FCNPI), CNPIFE (NN-PFH-ICG-Fe_3O_4, CNPIFE) and CNPI (CN-PFH-ICG, CNPI) were similar with FCNPIFE, except the dispose of SPIONs for FCNPI, the replacement of DSPE-PEG2000-FA with DSPE-PEG2000 for CNPIFE, and the combination of the two mentioned above adjustments for CNPI.

Characterization of FCNPIFE Liposomes

The morphology of FCNPIFEs was observed by transmission electron microscope (TEM). The size distribution and zeta potential of FCNPIFEs dissolved in PBS were measured by Laser Particle Size Analyzer System (Mastersizer 3000, Malvern, USA) at 4°C within 7 days. To verify whether ICG was successfully loaded in FCNPIFE, the absorption spectra of different nanoparticles (FCNPIFE, FCNPFE, FCNPI, CNPIFE, FCNIFE, CNPI and ICG) were detected by an ultraviolet spectrophotometer (260-Bio, Thermo Fisher Scientific). The loading efficiency and loading content of ICG were calculated based on the following formulas:

Loading efficiency (%) = (total ICG - unbound ICG)/total ICG

Loading content (%) = (total ICG - unbound ICG)/total liposomes.

After dissolved in 2% nitric acid solution, the Fe content in FCNPIFEs was detected by inductively coupled plasma atomic emission spectroscopy (ICP-AES), and the encapsulation efficiency and encapsulation capacity of Fe_3O_4 were calculated by the following formulas:

Encapsulation efficiency (%) = mass of Fe_3O_4/total Fe_3O_4 input

Encapsulation content (%) = mass of Fe_3O_4/total nanoliposomes.

The magnetic properties of the FCNPIFEs were studied by vibrating sample magnetometer (VSM, Lake Shore 7404, USA) at a temperature of 300 K. To further explore the magnetic-target performance, the FCNPIFEs solution was resuspended in a small glass bottle on which side placed a magnet (4 T) for 6 h, and observed the aggregation of nanoparticles in the magnetic field area. In addition, the phase transition of FCNPIFEs under 808nm laser irradiation was recorded by confocal microscopy. After oxygenating FCNPIFEs, FCNIFEs, and PBS for 10 min, 1 mL of each was added to the degassed water, then the mixture was placed in a 47°C water bath for 10 min to test the oxygen-carrying capacity of PFH. Finally, a portable dissolved oxygen meter (550A, YSI, Ohio, USA) was used to monitor the dissolved O_2 concentration in these liposome solutions.

Cell Culture

The RPMI-1640 medium containing 20% FBS and 1% penicillin/streptomycin was used to culture the human retinal pigment epithelium cell line ARPE-19 and the human RB cell line Y79 at 37°C and 5% CO_2. Both cell lines were purchased commercially from Shanghai Baiyi Biotechnology Center.

Animal Model

All animal experiments and procedures were carried out in accordance with the protocols approved by the Animal Ethics Committee of Chongqing Medical University and Guide for the Care and Use of Laboratory Animals. To establish the retinoblastoma tumor model of nude mice (female, 6–8 weeks old), Y79 cells were suspended in PBS (1×10^6 cells in 100μL per mouse) and subcutaneously injected into the thigh of the nude mice.[40]

Vitro and in vivo Targeting Efficiency

After being labeled with Dil, the CNPI, CNPIFE, FCNPI, FNNPIFE, and FCNPIFE were seeded with Y79 cells into 6-well plates (2×10^5 cells per well), and groups were divided as follows: control group, CNPI, folate (FA)+FCNPI, CNPIFE+magnetic field (M.F), FCNPI, FNNPIFE+M.F, FCNPIFE+M.F. Magnetic field was performed by a magnet (approximately 4 T) attached to the side of wells and the incubation was kept for 1, 3 and 6h. After those incubations were finished, the cells were fixed with paraformaldehyde for 15 min, then incubated with DAPI and DIO for 15 min to stain the nuclei and membranes, respectively. The intracellular absorption behavior of nanoparticles in every group was observed by confocal microscopy, and quantitative analysis of the seven groups (n = 3) was conducted by flow cytometry.

Y79 tumor-bearing mice were randomly divided into 6 groups (n = 3): group(I): CNPI, group (II):CNPIFE, group(III):CNPIFE+M.F, group(IV):FCNPI, group(V):FNNPIFE+M.F, group(VI):FCNPIFE+M.F. And all injected nanoparticles were labeled with DiR. Magnets (approximately 4T) were applied to the relevant groups, and the fluorescence system was used to obtain the fluorescence images (excitation 750 nm/emission 780 nm) of all groups at different time points post-injection of nanoparticles (0, 3, 6, and 24 h). Finally, tumors and major organs of the mice were collected for fluorescence imaging, and corresponding fluorescence signals were analyzed.

In vitro and in vivo Multimodal Imaging

In vitro US image effect of FCNPIFEs was explored by MyLab 90 (Esaote, Italy). FCNPIFEs were diluted (0, 0.4, 0.8, 1.2 and 2.4 mg/mL) and exposed to 808 nm laser for 5min (1.5 W/cm^2). DFY (Institution of US Imaging of Chongqing Medical University, Chongqing, China) software was used to analyze the signal intensity generated from laser excitation. To evaluate the in vitro PA function of FCNPIFEs, FCNPIFEs were firstly diluted according to ICG concentrations (0.025, 0.05, 0.1, 0.2 and 0.4 mg/mL). Together with FCNPFE (ICG concentrations:0 mg/mL), the diluted FCNPIFEs were added to agar gel models separately. PA values of FCNPIFEs were recorded and analyzed by the VEVO LASR PA imaging system. To assess the function of MR imaging in vitro, the different concentration of FCNPIFEs (Fe concentration: 0.015, 0.03, 0.06, 0.12, 0.18 and 0.24 mM) were placed in EP tube. T2WI images were obtained using the TX Philips Achieva 3.0 T MR. The scanner (Philips Medical System, Netherlands) and the signal intensity (SI) of the region of interest (ROI) were analyzed by Sante DICOM with the following T2 parameters: TSE-T2WI, TR = 3800 ms, TE = 96 ms, Field = 3T, DFOV = 211 *250 mm, NEX = 2, matrix = 384*384, and Slice Thickness = 2.0 mm.

To test the in vivo US imaging effect of nanoparticles, three groups were divided as follows (n = 3): FCNPIFE+M.F, CNPI, FCNIFE+M.F. All groups were injected with 200 μL of corresponding nanoparticles (0.4 mg/mL), and the magnetic fields were performed by magnets (approximately 4T) fixed on the tumors. Before and after the excitation of 808 nm laser (1.5 W/cm^2) for 10 min, the images were simultaneously captured by the MyLab 90 in B-mode and CEUS-mode, while the average echo intensities were quantitatively analyzed by DFY. The grouping of in vivo photoacoustic imaging is similar with that of in vivo US imaging, except for replacing the FCNIFE+M.F group with the FCNPFE+M.F group. The images of three groups were captured and analyzed by the VEVO LASR PA imaging system at different time points (0, 3, 6 and 24 h). To test the in vivo MR imaging effect of nanoparticles, Y79 tumor-bearing nude mice were divided into two groups (n = 3): FCNPIFE+M.F and FCNPI. Philips Achieva 3.0 T TX

MR scanner was used to record T2WI images at different time points (0, 3, 6, and 24 h), and Sante DICOM was used to analyze ROI signals. T2-weighted images were obtained using the following parameters: TSE-T2WI, the volume coil (Shanghai Chenguang Medical Technology Co, China), TR = 5560 ms, TE = 85 ms, Field = 3T, DFOV = 80 *80 mm, NEX = 2, matrix = 384*384, and Slice Thickness = 0.7 mm.

Photothermal Properties, Photodynamic Properties, and Cytotoxicity in vitro

PBS, FCNPFE (0.4 mg/mL) and different concentration of FCNPIFE (0.05, 0.1, 0.2, 0.4 mg/mL) were irradiated with 808nm laser for 5 min (1.5 W/cm^2), and the different power (0.5, 1, 1.5, 2.0 W/cm^2) of irradiation was performed for 5 min on the FCNPIFE solution with a fixed concentration of 0.4 mg/mL. The thermal infrared imaging camera was used to record these temperature changes per second to draw the temperature rise curve within 5min and capture the thermal image per minute. The photothermal stability of FCNPIFE (0.4 mg/mL) was assessed by being exposed to the repeated five cycles of irradiation. To further verify that liposome encapsulation could improve the photothermal stability of ICG, changes of FCNPIFE, FCNPFE, and ICG before/after laser irradiation were recorded in UV absorption spectra. Finally, we, respectively, calculated the photothermal conversion efficiency (η) of FCNPIFE and ICG based on research of Liu[41] as follows:

$$\eta = \frac{hA\Delta T_{max} - Q_{Dis}}{I\left(1 - 10^{-A_{808}}\right)}$$

h: Heat transfer coefficient; *A*: Surface area of the container; *ΔTmax*: Temperature change of the NPs solution at maximum steady-state temperature; *I*: Laser power; A_{808}: Absorbance of different NPs at 808 nm; Q_{Dis}: Heat associated with the light absorbance of the solvent.

The generation of intracellular ROS was evaluated using DCFH-DA. Y79 cells were incubated with FCNPIFE (0.4 mg/mL), FCNIFE (0.4 mg/mL), and ICG (0.4 mg/mL) into 24-well plates (2 × 10^5 cells per well) for 3h under 4T magnetic field then irradiated by 808 nm laser (1.5 W/cm^2) for 5min. After the irradiation, DCFH-DA was added and incubated for 30 min. The ROS production was observed by confocal microscopy and quantitatively analyzed by flow cytometry. In addition, the corresponding hypoxic experiments were conducted in GENbox Jars.[31]

The biosafety of FCNPIFEs in vitro was studied by the CCK-8 method. Y79 and ARPE-19 cells were seeded in 96-well plates (1 × 10^4 cells per well) and cultured for 24 h. Then the medium was replaced with fresh medium containing FCNPIFEs at different concentrations (0.2, 0.4, 0.8, 1.2 and 1.6 mg/mL). After 24h incubation was finished, 20μL of the CCK-8 assay reagent was added to each well and incubated for 1h. The absorbance of each well at 450 nm was measured by a microplate reader (EL×800 Universal Microplate Reader, BIO-TEK Instrument Inc. USA).

To determine the optimal concentration of FCNPIFE for treatment, Y79 cells were seeded in 96-well plates (1 × 10^4 cells per well) and cultured for 24 h. Then the medium was replaced with fresh medium containing FCNPIFEs at different concentrations (0.1, 0.2, 0.4, 0.8 and 1.6 mg/mL). After incubation for 3h, each well was irradiated with 808nm laser for 5 min (1.5 W/cm^2), then incubated with 20 μL CCK-8 assay reagent for 1h. The absorbance of each well at 450 nm was measured by a microplate reader (EL×800 Universal Microplate Reader, BIO-TEK Instrument Inc. USA).

To verify the synergy between PDT and PTT, Y79 cells were seeded in 24-well plates (5 × 10^4 cells per well) and co-incubation with FCNPIFEs for 3h. The cells were divided as follows: control group, PDT group, PTT group PDT +PTT group, and each group was treated under normoxia and hypoxia conditions, respectively. According to the previous study,[31] the PDT effect of FCNPIFEs was manipulated by placing the culture dishes in ice bath to avoid the photothermal effect, and the PTT effect was manipulated by adding NaN_3 (100 mM) to avoid the photodynamic effect. Then, each group was stained with Calcein AM and (CAM) propidium iodide (PI) (BD Biosciences, USA) and quantitatively analyzed by flow cytometry.

In vivo Therapy

When the tumor volume grows to 100 mm^3, Y79 tumor-bearing mice were randomly divided as follows(*n*=3): group(I): saline, group(II):laser, group(III): FCNPIFE+M.F, group(IV):ICG+laser, group(V): FCNIFE+M.F+laser, group (VI): FCNPFE+M.F+laser, group(VII): CNPI+laser, group(VIII):FCNPIFE+M.F+ intermittent laser, group (IX): FCNPIFE +

M.F+laser. After the nanoparticles were injected into the tail veins for 6h (200 µL, 0.4 mg/mL), continuous laser irradiation (1.5W/cm^2) was applied to five relevant groups for 10 mi. Group(VIII) were exposed to intermittent laser for 20min (1.5W/cm^2, on 30s/off 30s) and the temperature was kept at 41°C to avoid the photothermal effect, so that group(VIII) could be treated with a single PDT treatment. Thermal imaging and temperature changes of groups under irradiation were recorded by infrared thermography. Relative tumor volumes and weight of nine groups were recorded every 2 days, and tumor inhibition rate was calculated based on the tumor volume data.

On the 3rd day post-therapies, major organs and tumors were harvested for hematoxylin and eosin (HE), proliferating cell nuclear antigen (PCNA), and terminal deoxynucleotidyl transferase-mediated dUTP-biotin nick end labeling (TUNEL) staining to evaluate the histological changes, the proliferation and apoptosis levels in different groups.

Mechanism of PTT/PDT Synergistic Therapy Produced by FCNPIFEs

In order to monitor the oxygenated hemoglobin saturation level in the tumor, the Y79 tumor-bearing nude mice were randomly divided into three groups (*n*=3): saline, the FCNIFE+M.F+laser group, the FCNPIFE+M.F+laser group. After injection of nanoparticles for 6 h, the mice were exposed to 808 nm laser for 10 min (1.5 W/cm^2), and the images in OXY-HEM mode and blood oxygen saturation (SO_2 average) were observed using the VEVO LASER PA imaging system. At 24h post-treatment, the tumors were fixed with 4% formalin and stained with HIF-1α (hypoxia induced factor, HIF).

To analyze the effect of photodynamic therapy on hyperthermia, the expression levels of HSP70 in the tumors were assessed using immunofluorescence staining. Nude mice of Y79 were randomly divided into four groups: saline, FCNIFE+M.F+laser, FCNPIFE+M.F+laser, and FCNPIFE+M.F. After injection of nanoparticles for 6 h, the groups receiving laser were exposed to 808nm irradiation for 10min (1.5 W/cm^2). At 24 h post-treatment, the tumors were harvested for HSP70 immunofluorescent staining and quantitative fluorescence analysis.

In vivo Biocompatibility Evaluation

On the 3rd day after treatment, the mice's major organs (heart, liver, spleen, lung, and kidney) were collected and collected for HE staining. To further assess the in vivo biosafety of FCNPIFEs, 12 female nude mice were injected with 200 µL of FCNPIFEs (0.4 mg/mL), and blood samples (*n*=3) at 0, 1, 7 and 14d were collected for routine blood and serum biochemistry tests.

Statistical Analysis

Data were expressed as mean ± standard deviation. Student's *t*-test and two-way analysis of variance were utilized to determine the statistical significance for two groups and for multiple groups, respectively. P values <0.05 were regard statistically significant (ns, no significance, *p < 0.05, **p < 0.01, ***p < 0.001, ****p < 0.0001).

Results and Discussion

Synthesis and Characterization of FCNPIFEs

Low magnification transmission electron microscopy (TEM) showed the successful synthesis of the FCNPIFEs, which possessed good dispersion and uniform sizes (Figure 1A). High magnification TEM further showed the structure of FCNPIFE more clearly that SPIONs, presented as small dark dots, were encapsulated in the outer edge of grey spherical surfaces (Figure 1A). The average diameter of the FCNPIFEs was (338.63 ± 10.90) nm and the zeta potential was (31.86 ± 3.49) mV (Figure 1B). Furthermore, no significant size and potential changes were observed during seven days, demonstrating the good stability of the nanoparticles (Figure 1C). The above results indicated that stable FCNPIFEs were successfully fabricated. Moreover, the average size of FCNPIFE could ensure a high permeability and retention efficiency, which were conducive to the accumulation of nanoparticles in tumor tissues.[42]

All nanoparticles except FCNPFEs appeared the characteristic absorption peaks at 779 nm in UV–vis–NIR absorption spectrum, suggesting the successful loading of ICG on these nanoparticles (Figure 1D). The ICG loading efficiency and loading content of FCNPIFEs were about 93.09% ± 0.63% and 15.51% ± 0.11wt%, respectively, based on the UV–vis–NIR

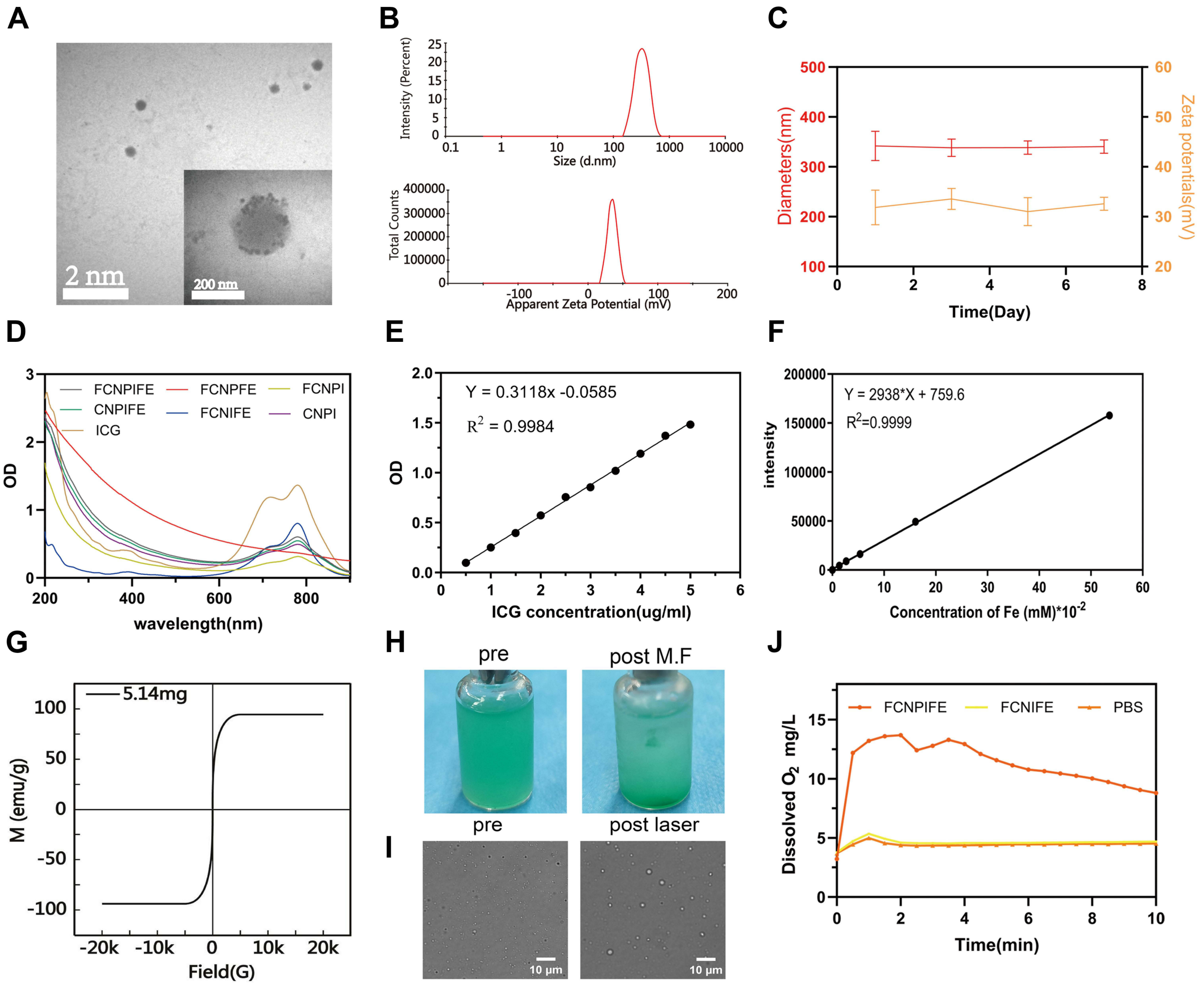

Figure 1 Characterization of FCNPIFE. **(A)** Low and high magnification TEM images of FCNPIFE (scale bar: 200 nm and 2 μm). (**B**) Representative diameters and zeta potentials of FCNPIFE. (**C**) The stability of FCNPIFE based on average diameters and zeta potentials. (**D**) UV–vis–NIR spectra of FCNPIFE, FCNPFE, FCNPI, CNPIFE, FCNIFE, CNPI and ICG. (**E**) The optical density of ICG (0.025, 0.05, 0.1, 0.2 and 0.4 mg/mL) in UV spectrophotometry. (**F**) The emission intensity of Fe (0.015, 0.03, 0.06, 0.12, 0.18 and 0.24 mM) in ICP-OES. (**G**) The magnetization curve of FCNPIFEs. (**H**) The aggregation effect of FCNPIFEs in the glass bottle before and 6h post-application of M.F. (**I**) CLSM images (scale bar: 10 μm) of the FCNPIFE phase transition before and 5min post-laser. (**J**) O_2 concentration changes among the FCNPIFE, FCNIFE and PBS under air-tight conditions.

calibration curve of ICG (Figure 1E). To verify that Fe_3O_4 was encapsulated into FCNPIFEs, ICP-OES was used to analyze emission intensity of FCNPIFEs with different concentrations (Figure 1F). The encapsulation efficiency and encapsulation content were calculated as 4.37% ± 0.80% and 0.0026% ± 0.05wt%, based on the ICP-OES result. Figure 1G shows that magnetization intensity of FCNPIFEs reached a saturation point at 91.84 emu/g and no coercivity or residual magnetism was founded in the hysteresis curve, suggesting that FCNPIFEs were superparamagnetic nanoparticles. After 6 h magnetic field application (approximately 4 T), FCNPIFEs were obviously concentrated on one side of the bottle, indicating that FCNPIFE has a certain magnetic targeting ability (Figure 1H). The load of PFH in FCNPIFEs was confirmed by capturing the phase-transition generated from 808 nm laser irradiation (1.5 W/cm^2, 5 min). Figure 1I shows that approximate 1um microbubbles were produced from FCNPIFEs after exposing to laser, which could improve US imaging performance.[30] The above-mentioned results demonstrated that ICG, PFH and Fe_3O_4 were successfully loaded into FCNPIFEs.

The different changes of oxygen concentration among FCNPIFEs, FCNIFEs and saline in degassed water proved that PFH was an efficient reservoir of O_2. Under the constant external heat (47°C,10min), the dissolved oxygen concentration of FCNPIFEs exhibited a rapid increase from 3.21 to 13.20 mg/mL within 60 seconds, then maintained at a higher concentration than FCNIFE and PBS in 10min (Figure 1J). These results were attributed to the pyrolysis of plentiful nanoliposomes, resulting in a blasting release of abundant O_2 pre-stored in oxygenated PFH. Although oxygen concentration of FCNIFEs increased within 1 min, it quickly reduced to equilibrium due to the lack of PFH (Figure 1J). All the above data indicated that PFH could be used as splendid oxygen storage material, conducive to the subsequent treatment experiments under hypoxic conditions.

Folate/Magnetic Dual-Targeting Ability of FCNPIFEs

To explore the most efficient cellular uptake in Y79, we compared the effect of folate/magnetic dual-target cationic nanoliposomes with that of folate/magnetic dual-target normal nanoliposomes, single target nanoliposomes, and non-target nanoliposomes. And the Confocal laser scanning microscope (CLSM) images were captured as shown in Figure 2A. The green and blue channels represented the cytomembranes and nuclei of Y79 cells, respectively, and the relevant nanoparticles were labeled red. The CNPI group and the FA+FCNPI group both showed rare red dots while the FCNPI group exhibited a stronger red fluorescence intensity after 3h incubation, suggesting that single folate-target slightly enhanced the intracellular endocytosis behavior. No obvious differences in red fluorescence intensity were observed between the CNPIFE+M.F group and the FCNPI group, demonstrating that single magnetic-target could promote the phagocytosis efficacy, nevertheless the effect is also limited and cannot be compared with that of dual-target groups. The folate/magnetic dual-target group contained the FCNPIFE+M.F group and the FNNPIFE+M.F group, and both groups performed well. However, it is worth noting that the former achieved the most efficient cell uptake of nanoparticles by Y79 cells. The excellent endocytosis efficiency of FCNPIFE+M.F group could be attributed to the electricity absorption on cell surface by cationic liposomes.[37] The flow cytometry results further confirmed our CLSM results. After 3h incubation with corresponding nanoplatforms, the FCNPIFE+M.F group displayed the most superior

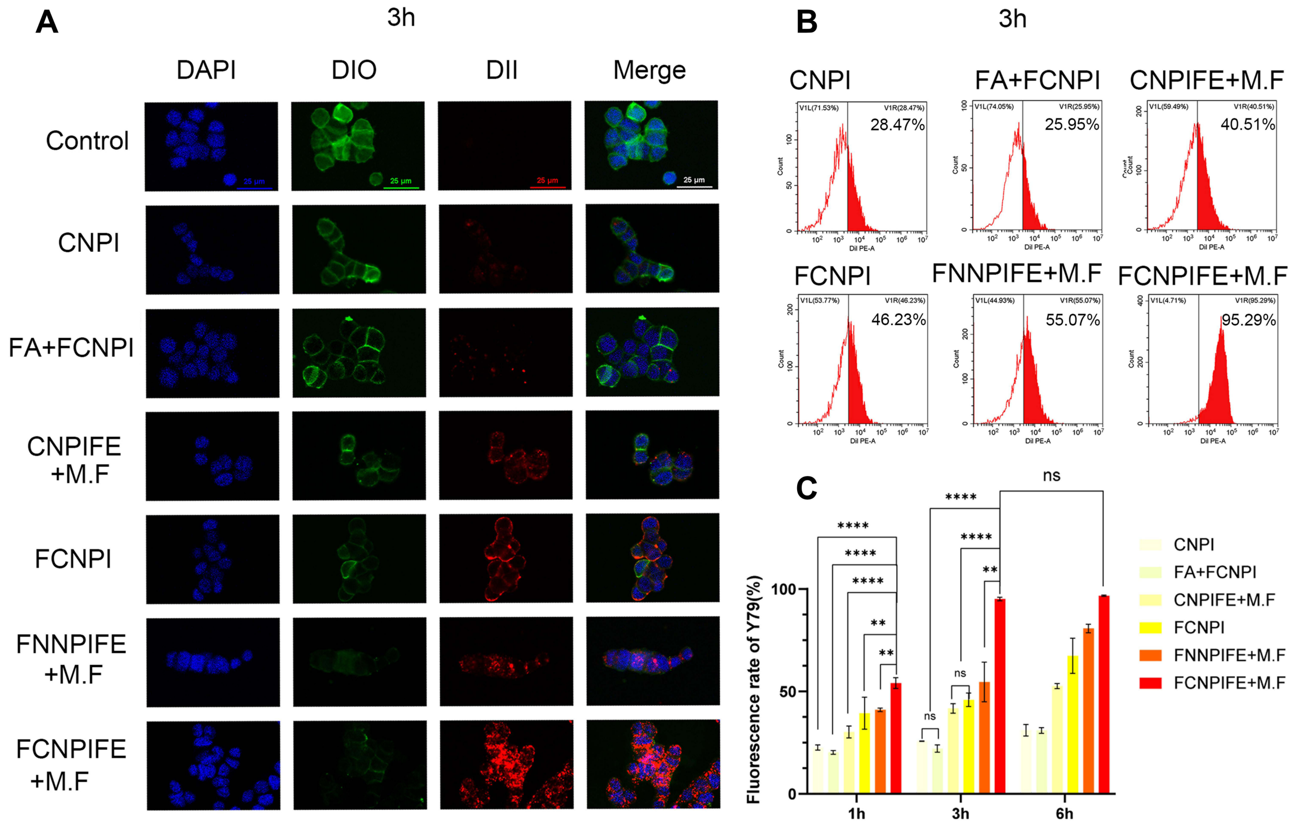

Figure 2 Intracellular uptake of FCNPIFE. (**A**) CLSM images (scale bar: 25 μm) of intracellular in different groups at 3 h. (**B**) Representative flow cytometric results of intracellular uptake in different groups at 3 h. (**C**) The quantitative flow cytometry analysis of intracellular uptake in different groups at 1 h,3 h and 6 h (n=3, $^{**}p < 0.01$, $^{****}p < 0.0001$).

targeting performance toward Y79 cells (Figure 2B). In order to deeply understand the targeting performance differences in the six groups, flow cytometry was used to quantitatively analyze the endocytosis rates at different time points (Figure 2C). The cell endocytosis rates of the FCNPIFE+M.F group have preceded other groups at 1h. Moreover, it reached a saturation firstly at 3h when intracellular endocytosis rates of other groups were almost no more than 50%. Those data further verified the advantages of FCNPIFE in targeting ability compared with other nanoparticles. By integrating these advantages, including the high specificity and sensitivity of folate-target, the unrestricted properties of magnetic-target that free from limits of individual differences in receptor expression, and the higher intracellular uptake achieved by cationic liposomes, into one nanoplatform, FCNPIFE significantly facilitated its accumulation in tumor regions, laying the foundation to maximize the therapeutic effect.

The fluorescence imaging results of Y79 tumor-bearing mice showed a similar tendency to in vitro experiments. As shown in Figure 3A, the fluorescence signal of FCNPIFE+M.F group firstly appeared at 3h post-injection, reached a peak at 6h and maintained a high fluorescence energy within 24h. In contrast, the first observation of fluorescence in other groups was delayed to varying degrees and all showed weaker fluorescence signals at 6h, suggesting inferior target abilities compared with the FCNPIFE+M.F group. Group (III) and group (IV) had no fluorescence signal at 3 h and 6 h,

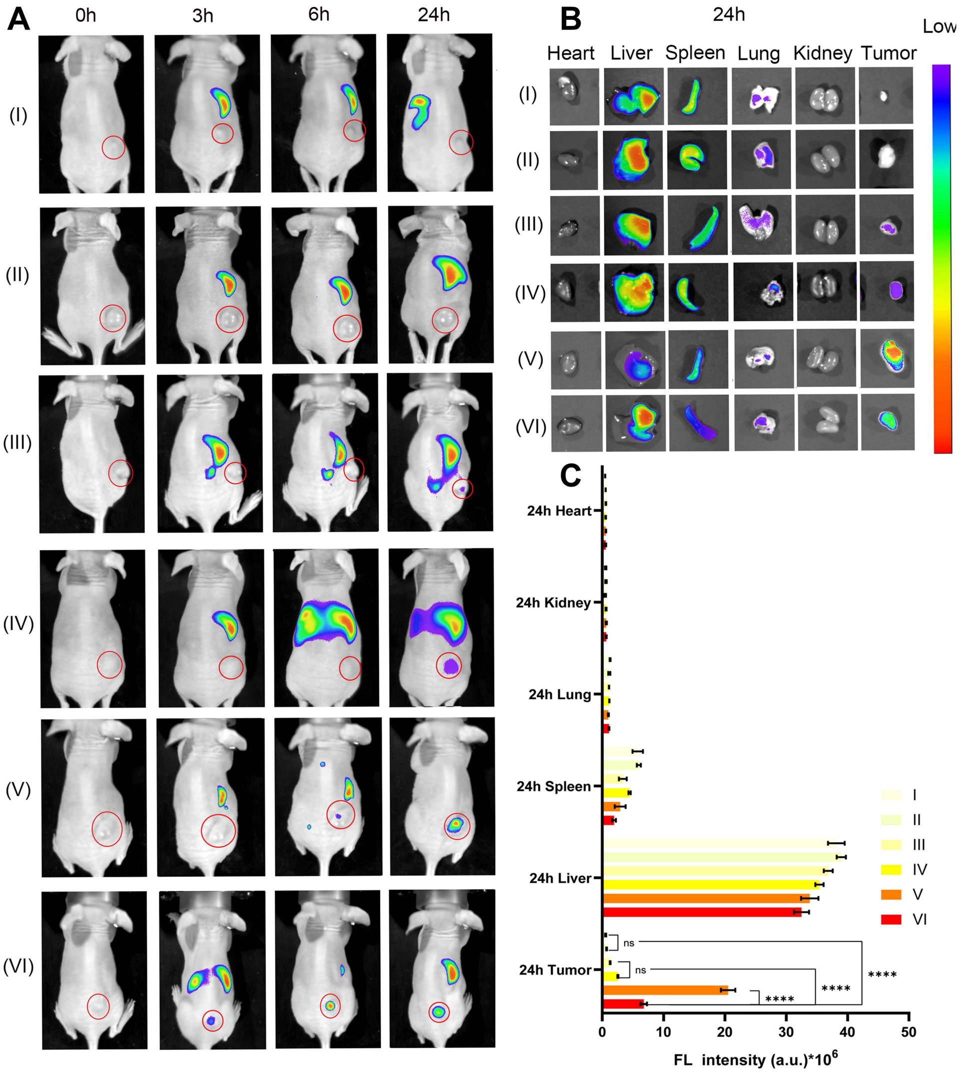

Figure 3 Fluorescence imaging and biodistribution of FCNPIFE. (**A**) FL images of Y79 tumor-bearing mice at 3 h,6 h and 24 h after injections of corresponding nanoparticles. Group (I): CNPI, group (II): CNPIFE, group (III): CNPIFE +M. F, group (IV): FCNPI, group(V): FNNPIFE+M.F, group (VI): FCNPIFE+M. F. (**B**) Biodistribution of different DiR-labeled nanoparticles in major organs and tumors at 24 h post-injection. (**C**) Quantitative fluorescence intensity in tumors and major organs at 24 h after injections of corresponding nanoparticles. (*n*=3, ****p < 0.0001).

while weak fluorescence signal began to appear at 24 h. We believe that is because after 24 hours, the intratumoral accumulation of corresponding nanoparticles in the two single-target groups had just reached a fluorescence intensity level that could be detected by the in vivo fluorescence imaging system. Compared with the dual-target group (V) and (VI) that showing obvious advantages in targeting performance, the group (III) (single-magnetic-target) and group (IV) (single-folate-target) showed a much slower and weaker targeting performance. Group (VI) showed a better targeting performance than group (V), which is due to the electricity absorption on cell surfaces by cationic liposomes.[37] The above results suggested that compared with other groups, only group (VI) could play the best targeting role, reflecting the advantages of dual-target and the advantages of adding cationic liposomes based on the dual-target. Figure 3B exhibits the biodistribution of relevant nanoliposomes in major organs as well as tumors, and their fluorescence intensity was quantitatively analyzed using a fluorescence analysis system (Figure 3C). In major organs, only the liver was observed to have significant accumulations of nanoparticles. The accumulation trend of different nanoparticles in tumors at 24 h was consistent with the performance of fluorescence imaging. These results suggested that FCNPIFE could guarantee the cumulative efficiency in tumors with minimizing the damage to major organs.

In vitro and in vivo Multimodal Imaging

Molecular probe based on ultrasonic contrast agent plays an important role in early diagnosis of tumor.[43] After irradiated by 808 nm laser (1.5 W/cm^2) for 10 min, PFH encapsulated in the FCNPIFEs were activated by optical droplet vaporization (ODV) to enhance US imaging in the CEUS mode, and a linear signal of CEUS-mode increased along with the increasing concentration of FCNPIFEs (Figure 4A). US images of tumors in Y79 tumor-bearing mice are shown in Figure 4B. An obvious US signal after laser irradiation was captured in the CEUS-mode at the tumor site of the FCNPIFE+M.F group, by contrast the FCNPFE+M.F group and the CNPI group showed no obvious change in the echo intensity before/after irradiation (Figure 4C). The difference between the FCNPIFE+M.F group and the FCNIFE+M.F group suggested that PFH entrapped in FCNPIFEs could enhance US imaging after 808nm laser irradiation.

As a nascent biological imaging model, the sensitivity and contrast of PA imaging are much better than US imaging,[44] ensuring a more precise visualization of FCNPIFEs accumulated in tumors. The PA signal of FCNPIFEs was the strongest under the excitation wavelength of 740 nm, and it strengthened linearly with the increasing of ICG concentration in vitro (Figure 4D), showing the good PA properties of FCNPIFEs. It was worth noting that SPIONs were widely used as PA contrast agents in many research.[45] However, the PA signal of FCNPFE in this study was hardly observed, indicating that only ICG could act as a PA contrast agent in FCNPIFEs. This might be explained by the low iron encapsulation efficiency in FCNPIFEs. FCNPIFEs also performed well in PA in vivo experiments. Compared with the other two groups, the FCNPIFE+M.F group firstly showed PA signals at tumor region at 3 h, then peaked at 6 h and maintained a high level of fluorescence energy within 24 h (Figure 4E), showing a signal trend consistent with that of in vivo fluorescence imaging. Moreover, the quantitative analysis of PA signals indicated that the signal value of the FCNPIFE+M.F group was 3.24 times higher ($P<0.0001$) than that of the CNPI group and the FCNPFE+M.F group (Figure 4F). In contrast, no obvious PA signal was observed in the CNPI group and the FCNPFE+M.F group within 24 hours, which further verified the superior targeting performance of FCNPIFEs and suggested that the component ICG was the only reason for PA imaging. Based on the abovementioned results, FCNPIFEs could be considered as excellent PA contrast agents.

MRI is the most recommended imaging monitoring method for RB patients with eyeball preservation.[32] Following the design of FCNPIFEs, we tested its properties for T2-weighted (T2WI) MRI. As shown in Figure 4G, the brightness of transverse MRI contrast images of FCNPIFEs filled in Eppendorf (EP) tubes decreased with the increase of Fe concentration. The T2WI images and relevant quantitative analysis showed that the pseudocolor contrast effect in tumor and relative T2 relaxation rate of the FCNPIFE+M.F group reached a maximum ($P<0.0001$) at 6h post-injection (Figure 4H and I), producing significantly negative contrast enhancement in the tumor sites. On the contrary, no significant difference in the T2 signal value was observed in the FCNPI group. Those results demonstrated that SPIONs were the effective component of FCNPIFE to negatively enhance T2WI MRI, which confirmed the potential of FCNPIFE in T2WI imaging.

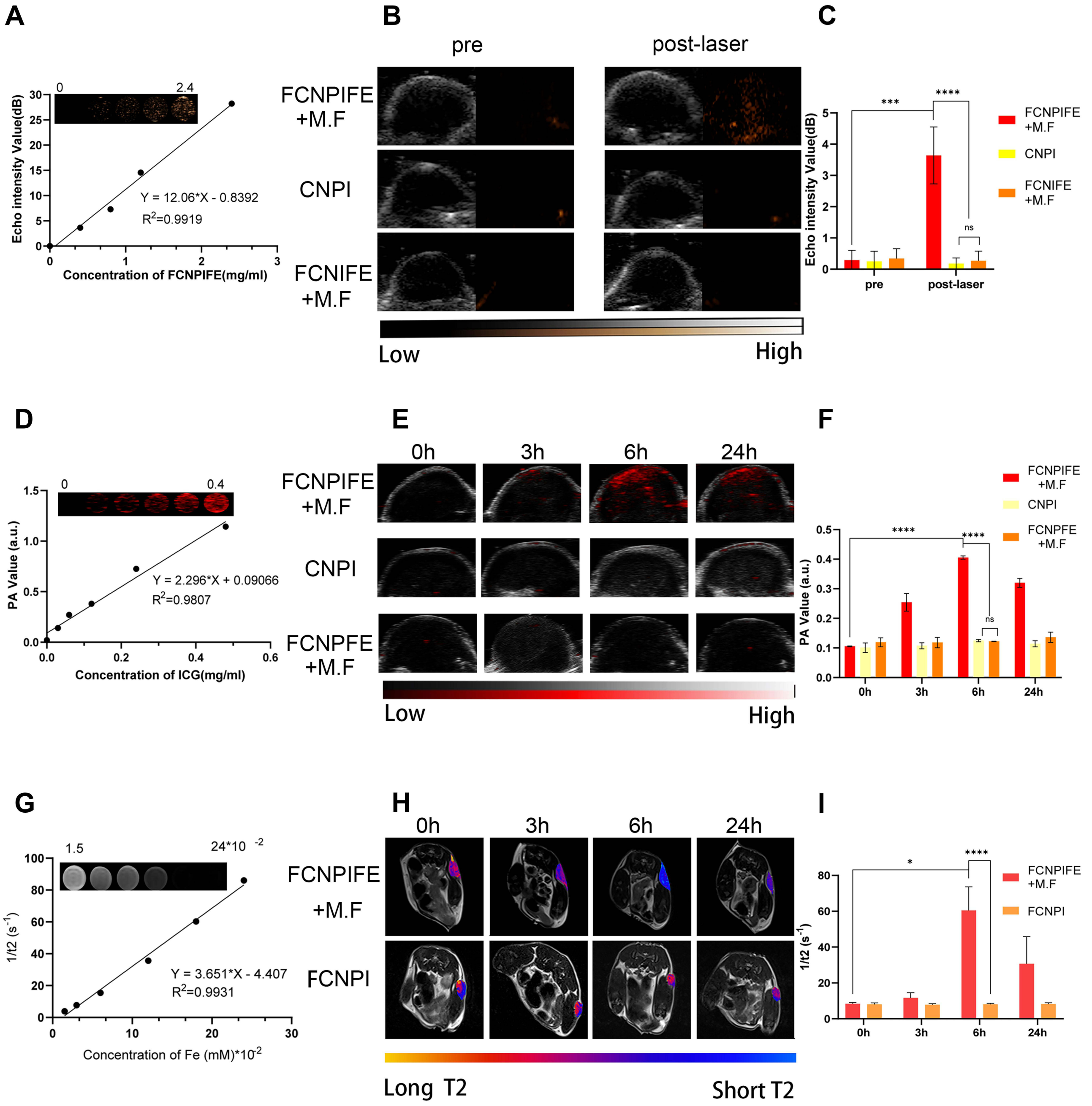

Figure 4 USI, PAI and MRI in vitro and in vivo experiments. (**A**) In vitro US images and echo intensity value of FCNPIFE. (**B**) US images of tumors in Y79 tumor-bearing mice with injections of FCNPIFE, FCNIFE, and CNPI before /after 808nm laser irradiation. (**C**) Corresponding echo intensities within tumor regions before/after 808nm laser irradiation (*n*=3, $^{**}p < 0.01$, $^{***}p < 0.001$). (**D**) In vitro PA images and PA value of FCNPIFE. (**E**) PA images of tumors in Y79 tumor-bearing mice after injections of FCNPIFE, CNPI and FCNPFE at different time points. (**F**) Corresponding PA intensities within tumor regions at different time points (*n*=3, $^{****}p < 0.0001$). (**G**) In vitro MRI and the transverse relaxivity (r2) of FCNPIFE. (**H**) T2 images of tumors in Y79 tumor-bearing mice after injections of FCNPIFE, FCNPI at different time points. (**I**) Corresponding signal intensities within tumor regions at different time points (*n*=3, $^{*}p < 0.05$, $^{****}p < 0.0001$).

In conclusion, FCNPIFE could achieve efficient accumulation in the tumor areas, and successfully showed the properties required for multimodal imaging. In addition, the optimal laser irradiation time window in further therapeutic experiments was determined as 6 h post-injection with the FCNPIFEs on account of those imaging results.

In vitro Photothermal Evaluation, Photodynamic Evaluation, and Cytotoxicity Studies

To make full sense of the FCNPIFE's therapeutic effect, the photothermal capacity was studied firstly. Under the same laser irradiation (1.5 W/cm^2,5 min), the temperature of FCNPIFEs solution diluted into a series of ICG concentrations (0.05, 0.1, 0.2 and 0.4 mg/mL) increased rapidly within 60 seconds, while PBS and FCNPFE did not show a significant warming trend during the whole irradiation process, indicating that FCNPIFEs had excellent photothermal properties (Figure 5A and B). Another noteworthy aspect was that the photothermal properties of FCNPFEs were almost absent, showing a temperature curve almost coincident with that of PBS (Figure 5B). Combined with the previous results of FCNPFE in PA experiment, this finding indicated that SPIONs only exhibited the properties required for targeting and MRI contrast agents, which was inconsistent with other researches using SPIONs as PTT agents and PA imaging contrast agents.[34,46] These unexpressed characteristics may correspond to the poor Fe_3O_4 loading efficacy in FCNPFEs. As shown in Figure 5C and D, the temperature rises also followed power-dependent and time-dependent manners with a fixed FCNPIFE concentration. Moreover, the good photothermal stability of FCNPIFEs has also been proved. Under five cycles of on-off laser irradiation, Figure 5E shows no obvious decrease in the peak temperature of FCNPIFEs. The property was further verified by the UV–vis–NIR absorption spectra (Figure 5F), in which the absorbance of FCNPIFEs and FCNIFEs reduced by nearly 32% while ICG reduced by 76% after 5min laser irradiation. The enhanced photostability of FCNPIFEs might be due to the protection of liposome encapsulation, thereby effectively decreasing water-induced ICG transformations,[47] which is profitable for the application of FCNPIFEs in subsequent experiments. The results of photothermal conversion efficiency also confirmed that FCNPIFE had stronger photothermal performance than ICG. The photothermal conversion efficiency of FCNPIFE was approximately 47.49%, while that of ICG was approximately 39.64%. From the above, FCNPIFEs can be considered as excellent NIR laser-induced photothermal materials.

Then the in vitro photodynamic properties of FCNPIFEs were analyzed by CLSM (Figure 5G) and flow cytometry. The similar fluorescence intensity of FCNPIFEs under hypoxia and normoxia suggested that the PDT effect of FCNPIFEs was not limited by hypoxia. However, compared with the fluorescence generated under normoxia, only weak green fluorescence was observed in FCNPFEs and ICG under hypoxia. The enhanced PDT effect of FCNPIFEs under hypoxia demonstrated that PFH could be used as an excellent oxygen reservoir, effectively alleviating the intracellular hypoxia and improving the PDT efficiency. What is more, FCNPIFEs always generated more ROS than ICG and FCNIFEs under identical conditions. The quantitative analysis of flow cytometry further confirmed the therapeutic advantage of FCNPIFEs under hypoxia (Figure 5H and I). The ROS produced by FCNPIFE under hypoxia was 6.46 times ($P<0.0001$) more than that of ICG, and 6.15 times ($P < 0.0001$) more than that of FCNIFE. Therefore, it is reasonable to think that FCNPIFEs displayed the potential to enhance the PDT effect by alleviating intratumoral hypoxia.

The unobvious cytotoxicity of FCNPIFEs without laser excitation was verified by CCK-8 in RPE and Y79 cells (Figure 5J). Even after the cells were co-cultured with 1.6 mg/mL FCNPIFE for 24 h, the cell viabilities of Y79 and RPE were not less than 90%. To balance the biosafety needs to avoid hyperthermia and the needs to maximize the therapeutic effect of FCNPIFEs, the dose of FCNPIFEs (0.4 mg/mL) and laser parameters (1.5 w/cm^2, 5 min) were determined for in vitro therapy. The CCK-8 results (Figure 5K) indicated that the 0.4 mg/mL group successfully displayed high cytotoxicity after 5min laser irradiation, remaining approximately 30.12% ± 1.96% cell viability. Compared with the group showing the strongest cytotoxicity, the difference in average cell mortality was less than 17% ($P<0.01$). Such results were acceptable, considering the biosafety required for in vivo application of FCNPIFEs.

To deeply understand how FCNPIFEs induced apoptosis in Y79 cells, flow cytometry was used to analyze the survival rate of Y79 cells in different groups (Figure 5L). Compared with the control group, the PDT group exhibited cell destruction rates total of 31.93% ± 2.8% ($P<0.0001$) under hypoxia, while the PTT group showed better therapeutic effects with cell destruction rates total of 56.37% ± 2.49% ($P<0.0001$). However, the strongest apoptosis effect was achieved by the PDT and PTT group, of which the cell destruction rates reached 67.1% ± 3.09% ($P<0.0001$). The results indicated that FCNPIFEs showed an enhanced synergistic therapeutic effect even under hypoxia. In addition, no significant difference was observed in the PDT group under hypoxia and normoxia, which was consistent with the in vitro photodynamic evaluation results. The CLSM images of CAM/PI visually demonstrated PTT/PDT synergistic

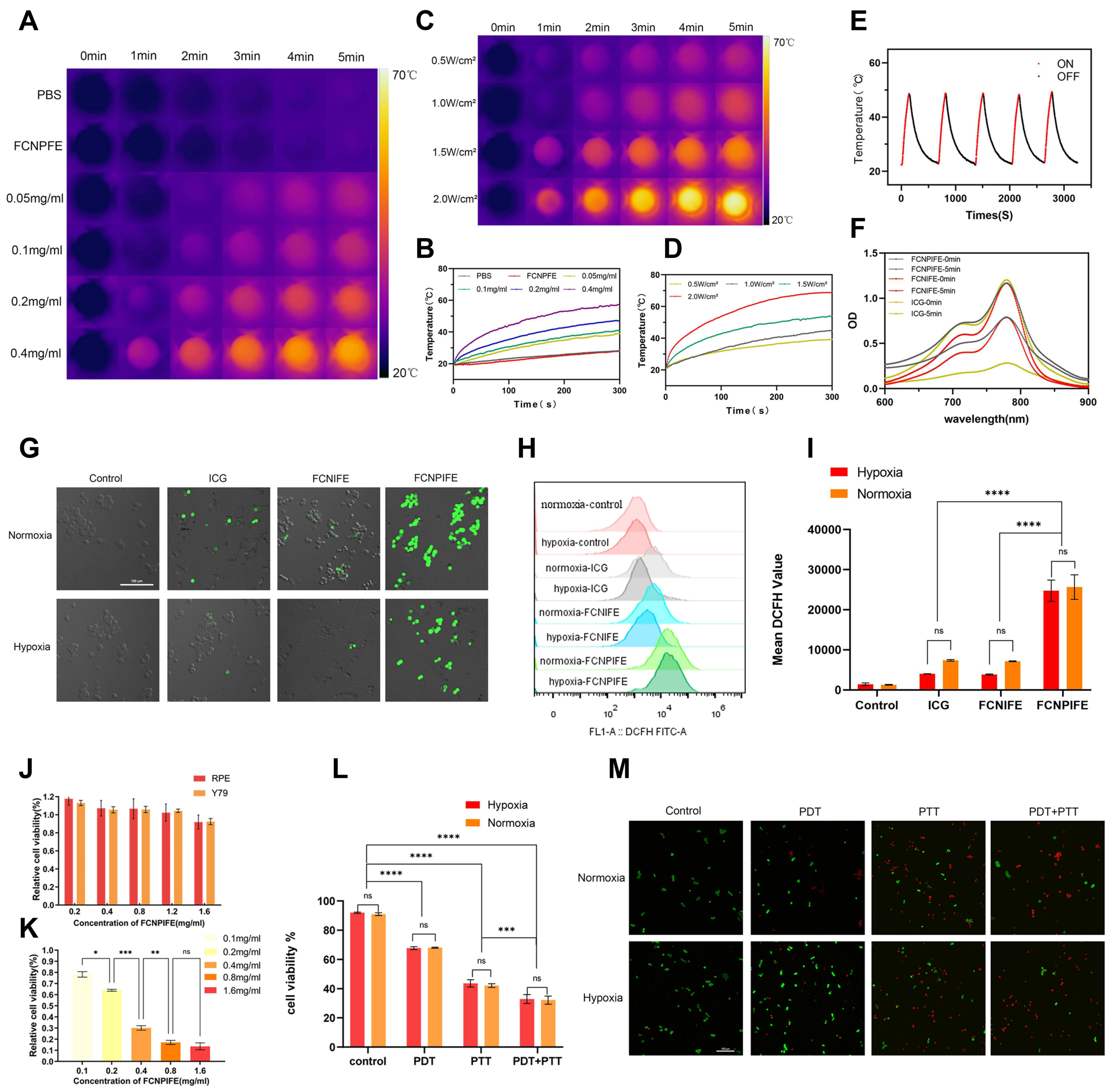

Figure 5 In vitro PTT, PDT performance and cytotoxicity of FCNPIFE. (**A**) Thermal images of PBS, FCNPFE and different concentrations of FCNPIFE under 808nm laser (1.5 W/cm^2, 5 min). (**B**) Photothermal heating curves of PBS, FCNPFE and different concentrations of FCNPIFE under 808 nm laser (1.5 W/cm^2, 5 min). (**C**) Thermal images of FCNPIFE (0.4 mg/mL) under different power of 808nm laser for 5 min. (**D**) Photothermal heating curves of FCNPIFE (0.4 mg/mL) under different power of 808nm laser for 5 min. (**E**) Photothermal stability of FCNPIFE under repeated five cycles of 808nm laser (1.5 W/cm^2; on 30s, off 30s). (**F**) UV–vis–NIR spectra changes of FCNPIFE, FCNIFE and ICG before/after 5 min of irradiation (1.5 W/cm^2). (**G**) CLSM images (scale bar: 100 μm) of intracellular ROS generated from ICG, FCNIFE and FCNPIFE under normoxic and hypoxic conditions. (**H**) The representative flow cytometry analysis of intracellular ROS generated from ICG, FCNIFE and FCNPIFE under normoxic and hypoxic conditions. (**I**) Quantitative flow cytometry analysis of ROS generated from ICG, FCNIFE and FCNPIFE in Y79 cells under normoxic and hypoxic conditions (*n*=3, ****p < 0.0001). (**J**) Cell viability of Y79 cells and ARPE-19 cells after incubated with different concentrations of FCNPIFE. (**K**) Cell viability of Y79 cells incubated with different concentrations of FCNPIFE after 5 min irradiation (*n*=3, *p < 0.05, **p < 0.01, ***p < 0.001). (**L**) Quantitative flow cytometry analysis of Y79 cells after PDT, PTT, and PTT+PDT under normoxic and hypoxic conditions (*n*=3, ***p < 0.001, ****p < 0.0001). (**M**) The Calcein-AM/PI staining images of Y79 cells after PDT, PTT, and PTT +PDT under normoxic and hypoxic conditions (scale bar: 100 μm).

therapy effects of FCNPIFE in Y79 cells (Figure 5M), showing an apoptosis tendency similar with that of flow cytometry analysis.

The above results demonstrated that, with excellent photothermal properties and enhanced photodynamic properties, FCNPIFEs could play a synergistic anticancer effect under hypoxia no inferior to that in normoxia.

In vivo Therapy

Motivated by the good anticancer efficacy of cellular therapy and the greatly enhanced tumor accumulation, we continue to evaluate the in vivo anticancer performance of PTT/PDT synergistic therapy produced by FCNPIFEs. Y79 tumor-bearing mice were randomly divided into nine groups: group(I):saline, group(II):laser, group(III): FCNPIFE+M.F, group(IV):ICG+laser, group(V): FCNIFE+M.F+laser, group(VI): FCNPFE+M.F+laser, group(VII): CNPI+laser, group-(VIII):FCNPIFE+M.F+ intermittent laser, group(IX): FCNPIFE +M.F+laser. It should be noted that due to the difference between in vivo and in vitro environments, the laser parameters in vitro could not produce a similar heating effect in vivo.[48] Therefore, we extended the laser time to 10min to make up for this defect.

Firstly, the temperature changes of groups treated with laser were recorded by an infrared thermal camera. As shown in Figure 6A, slightly gentle temperature rises were observed in the following four groups: the laser group, the ICG+laser group, the FCNPFE+M.F+laser group and the CNPI+laser group. And in the FCNPIFE+M.F+ intermittent laser group, the temperature was remained below 41°C to avoid the PTT effect (Figure 6B). On the contrary, in the FCNIFE+M.F +laser group and in the FCNPIFE+M.F+laser group, the local temperature increased sharply in one minute and the maximum temperature reached about, respectively, 47°C and 47.5 °C. The two almost coincident heating curves of the FCNIFE+M.F+laser group and the FCNPIFE+M.F+laser group demonstrated that there were similar photothermal therapeutic effects in the two groups. Infrared images visualized those abovementioned temperature changes (Figure 6C and D). In addition, the differences in temperature rise between the CNPI+laser group and the FCNPIFE +M.F+laser group reconfirmed the superior targeting performance of FCNPIFEs, which ensured the effective intratumoral accumulations in the FCNPIFE+M.F+laser group 6h post-injection.

To further verify the merits of PTT/PDT synergistic therapy produced by FCNPIFEs, tumor volumes of different groups were measured for 16 days (Figure 7A). Fast tumor growth trends were observed in the following six groups: the saline group, the laser group, the FCNPIFE+M.F group, the ICG+laser group, the FCNPFE+M.F+laser group, and the CNPI+laser group, showing an average 8–10-fold increase in the initial tumor volume and no significant difference was found among the six groups (Figure 7B). A mild tumor inhibition efficiency was achieved by the FCNPIFEs+M.F+intermittent laser (30s on/30s off) group, which produced photodynamic therapy alone and showed an average 4.6-fold growth in tumor volume, verifying that the oxygenated PFH encapsulated in FCNPIFEs could relieve low PDT efficiency under hypoxia, thus delaying

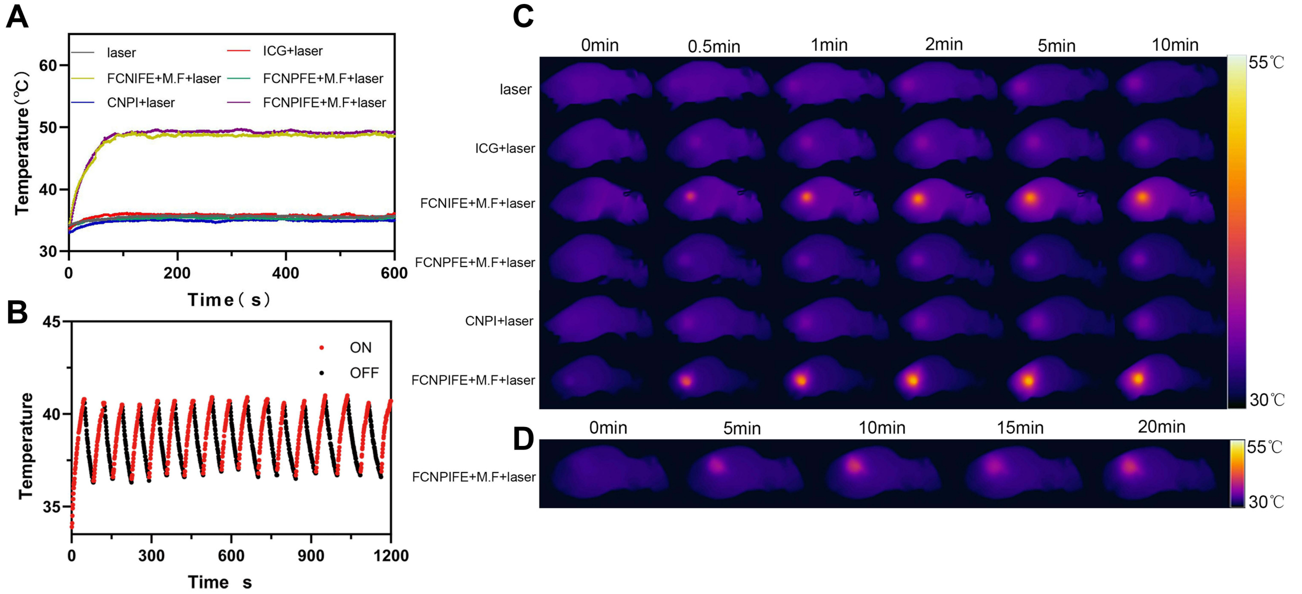

Figure 6 In vivo photothermal effects of different groups. (**A**) Photothermal heating curves of Y79 tumor-bearing mice in different groups irradiated by continuous laser (1 0.5W/cm^2, 10 min). (**B**) Photothermal heating curves of Y79 tumor-bearing mice treated with FCNPIFE+M.F+intermittent laser (1 0.5W/cm^2, on 30s/off 30s, 20 min). (**C**) Thermal images of Y79 tumor-bearing mice in different groups irradiated by continuous laser (1 0.5W/cm^{2,} 10 min). (**D**) Thermal images of Y79 tumor-bearing mice treated with FCNPIFE+M.F+intermittent laser (1 0.5W/cm^2, on 30s/off 30s, 20 min).

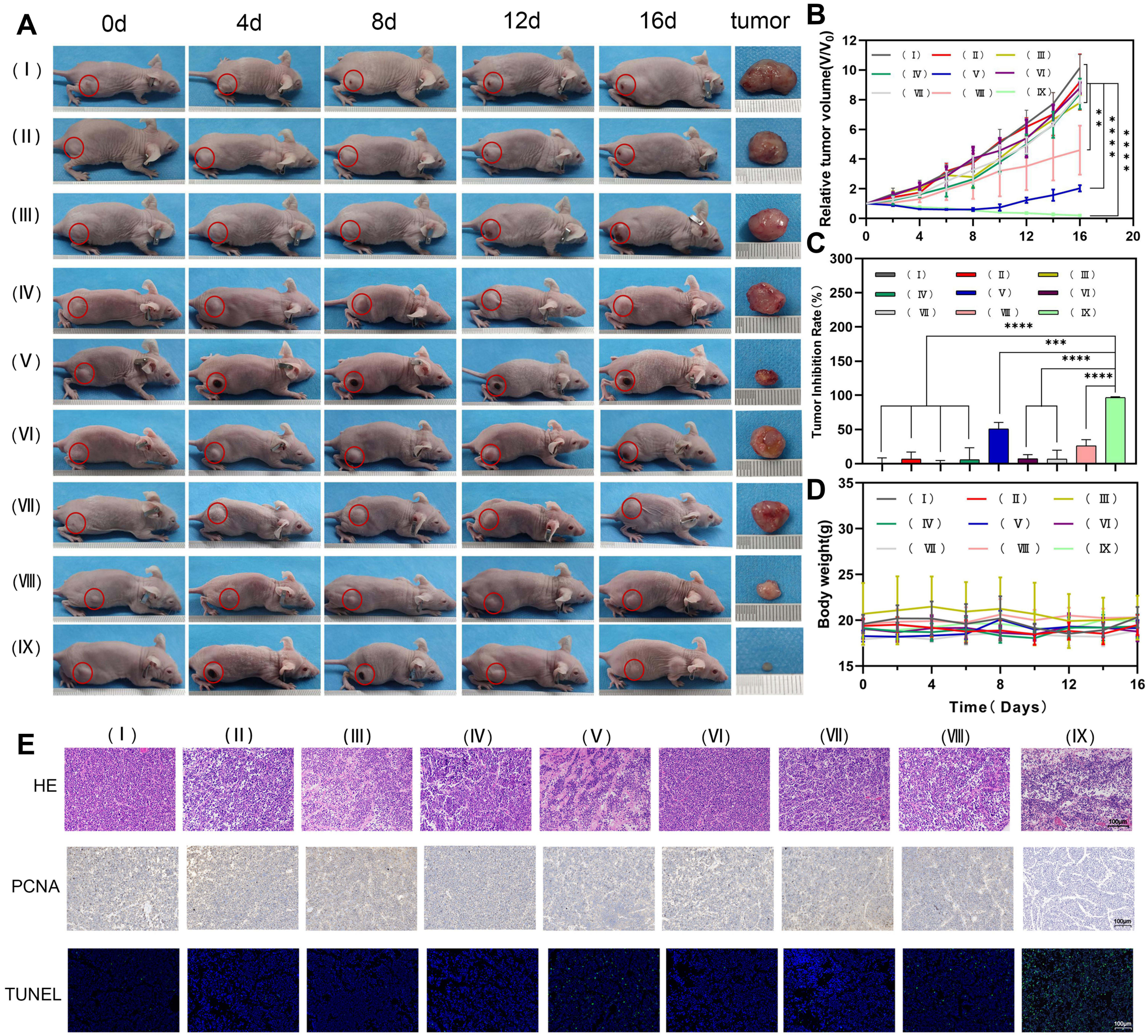

Figure 7 In vivo therapeutic effects of different groups. (**A**) Representative digital images of tumor-bearing mice in different groups. group(I):saline, group(II):laser, group(III): FCNPIFE+M.F, group(IV):ICG+laser, group(V):FCNIFE+M.F+laser, group(VI): FCNPFE+M.F+laser, group(VII):CNPI+laser, group(VIII):FCNPIFE+M.F+intermittent laser, group(IX): FCNPIFE+M.F+laser. (**B**) Time-dependent relative tumor volume(V/V0) curves of mice in the different groups (*n* =3, **p < 0.01, ****p < 0.0001). (**C**) Tumor inhibition rates of nine groups after receiving different treatments. (*n* =3, ****p < 0.0001). (**D**) Body weight curves of Y79 tumor-bearing mice for each group during the 16d period. (**E**) HE, TUNEL, and PCNA staining results of different groups on the 3st day post treatments (scale bar:100μm).

tumor growth to some extent. Lacking PFH, the FCNIFE+M.F+laser group could be considered as receiving PTT alone. It achieved the same excellent tumor inhibition effect as the FCNPIFE+M.F+laser group at 8d but regrew to average 2.04-fold volume at the end of therapy (Figure 7B), suggesting that though showing a better anti-tumor efficiency than the FCNPIFEs +M.F+intermittent laser group, the single PTT was also not insufficient to inhibit tumor growth completely.

Contributing to the oxygen supplement by PFH, the FCNPIFE+M.F+laser could be regarded as receiving PTT/PDT synergistic therapy and showed the most satisfactory anticancer effect compared with all other groups. As shown in Figure 7B, the FCNPIFE+M.F+laser group showed a continuous negative growth trend of tumor volume during the study and almost completely subsided on the 16th day (Figure 7A). Since the results of relevant heating curve in vivo have confirmed that the same photothermal effect in the FCNIFE+M.F+laser group and the FCNPIFE+M.F+laser group, it could be inferred that the curative efficacy of FCNPIFE+M.F+laser group was promoted by the enhanced PDT effect.

Based on those relative tumor volume data, the tumor inhibition rates of different groups were calculated (Figure 7C), and the FCNPIFE+M.F+laser group displayed the highest tumor inhibition rate among all groups ($P<0.0001$). Finally, no noticeable difference of weight changes among all groups was detected, implying that these nanoplatforms did not have significant systemic side effects in vivo (Figure 7D).

Analysis of the HE staining, TUNEL assay and PCNA assay at the 3rd day post-treatment further verified the treatment efficiency advantage of FCNPIFEs (Figure 7E). There was the most obvious apoptosis in the HE staining result of the FCNPIFE+M.F+laser group, followed by that of the FCNIFE+M.F+laser group. A mild injury was observed in the FCNPIFE+M.F+intermittent laser group, by contrast that the other 6 groups were not obviously affected by corresponding treatments. Moreover, the proliferation and apoptosis levels exhibited by PCNA and TUNEL were consistent with the results of HE staining. Overall, the FCNPIFE+M.F+laser group showed excellent oncotherapy potential through the PTT/PDT synergistic therapy without apparent systemic toxicity.

Mechanism of Synergistic PTT/PDT Synergistic Therapy Produced by FCNPIFEs

In order to further understand how the photothermal and photodynamic effects of FCNPIFEs produce the synergistic anticancer effect, we analyzed the enhanced photodynamic effects under hypoxia and the expression changes of HSP70 in synergistic therapy.

The PA imaging was used to observe the changes of oxygenated hemoglobin rate in tumors before/after 6h injections of saline, FCNIFEs, and FCNPIFEs. As shown in Figure 8A, the saline group and the FCNIFE+M.F group showed no significant change of tumor oxyhemoglobin signal under laser irradiation, while the FCNPIFE+M.F group exhibited a greatly enhanced signal intensity compared with that of the pre-state. The corresponding quantitative analysis (Figure 8B) showed that the blood oxygen saturation in the FCNPIFE+M.F group increased from 33.34% ± 2.91% to

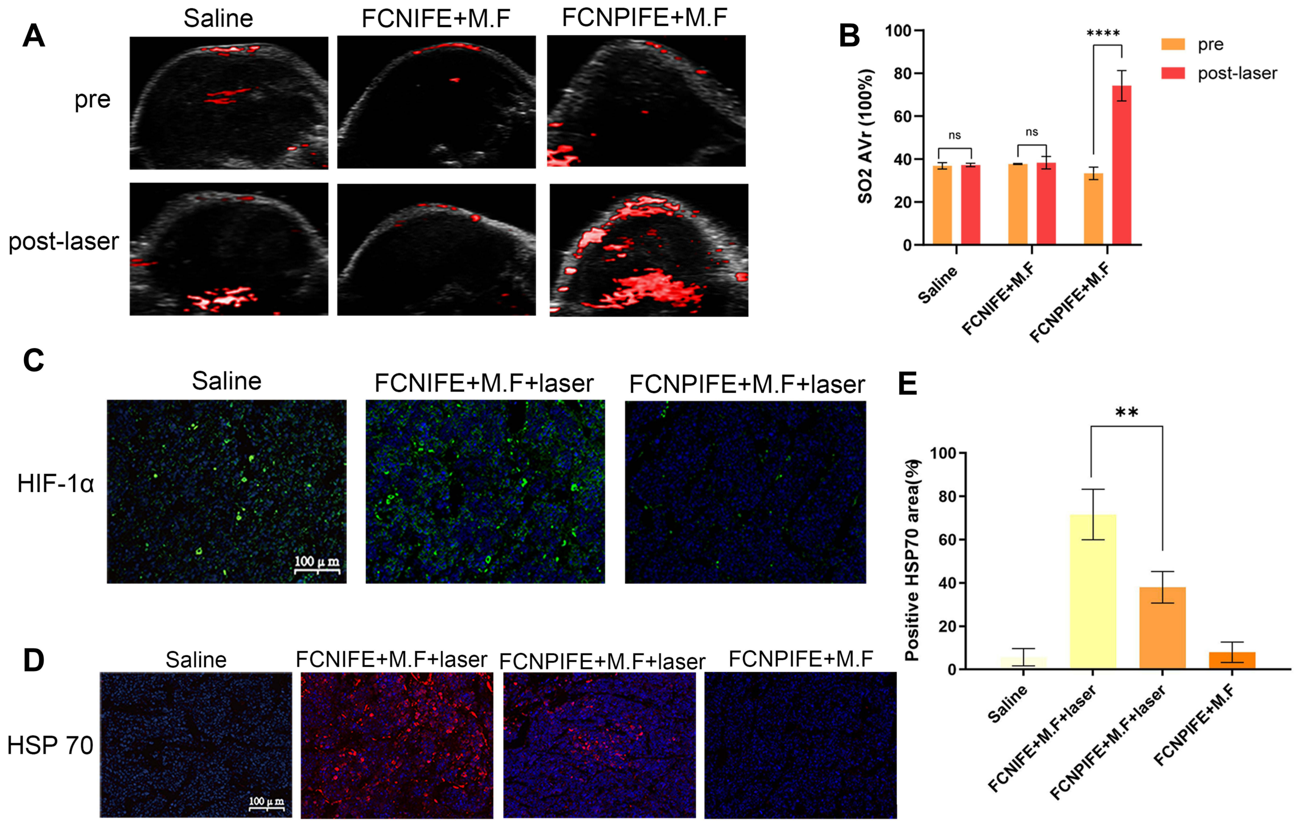

Figure 8 The mechanism behind synergistic therapeutic efficacy of FCNPIFE. (**A**) PA images of different groups in oxy-hemoglobin mode before/post-irradiation (1.5W/cm^2,10 min). (**B**) Quantification of oxyhemoglobin saturation in tumor regions of different groups (*n* =3, ****$p < 0.0001$). (**C**) HIF-1α immunofluorescent staining of tumors collected from different groups on the 1st day post-treatments. (**D**) HSP70 immunofluorescent staining of tumors collected from different groups on the 1st day post-treatments. (**E**) Quantitative analysis of HSP70 expression of different groups on the 1st day post-treatment (*n* =3, **$p < 0.01$).

74.21% ± 7.08% ($P<0.0001$), which significantly alleviated the hypoxia in the tumor. The HIF-1α immunofluorescence staining results further verified the therapeutic advantage of FCNPIFEs under hypoxia. As shown in Figure 8C, the FCNPIFE+M.F+laser group showed weaker green fluorescence than the other two groups, indicating lower expression of HIF-1α. Those results demonstrated that PFH encapsulated in FCNPIFEs could ensure oxygen supplement under hypoxia to reduce the expression of HIF-1α, thereby enhancing the photodynamic effect.

Then we discussed whether the enhanced PDT in FCNPIFEs benefited PTT efficacy in FCNPIFEs. Previous studies have confirmed that the expression of HSP70 could develop thermo-resistance for cells.[49] Therefore, it was necessary to reduce the expression of HSP70 during the treatment, which could guarantee the anticancer efficacy of PTT as much as possible. As shown in Figure 8D, the FCNPIFE+M.F+laser group exhibited less red fluorescence area compared with the FCNIFE+M.F+laser group, suggesting a lower HSP70 expression level with the assistance of PFH loaded in FCNPIFEs. According to the corresponding quantitative analysis (Figure 8E), the positive HSP70 area (%) of FCNPIFE was reduced by approximately 33.61% ($P<0.01$).

The impaired HSP70 expression level may be explained by the irreversible damage of ROS to mitochondria and metabolism, which restrained the HSP70 protein transcription,[38,50] and made tumor cells more sensitive to high temperature, thus achieving the synergistic PTT and PDT antitumor effects in FCNPIFEs.

Biosafety Assay

As shown in Figure 9A, the HE staining of major organs (heart, liver, spleen, lung, and kidney) in all the groups showed no obvious damage at the end of therapy. Additionally, complete blood count (WBC, Lymph, Mon, Gran, RBC, HGB, PLT), liver functional markers (ALT, AST, ALP), and kidney functional markers (BUN, CREA) showed negligible change during the study period, suggesting a strong in vivo biosafety of FCNPIFEs in treatment of RB (Figure 9B).

Animal Model

We chose the subcutaneous xenograft tumor model of nude mice with Y79 cells rather than the orthotopic tumor model to perform the in vivo experiment for several reasons. Firstly, compared to the subcutaneous xenograft tumor model, the early stage of orthotopic tumor was less intuitive in observation and quantitation, making it difficult to determine the appropriate time for in vivo experiments and to accurately evaluate the efficiency of in vivo therapy trials. Secondly, due to the small size of nude mice eyeballs, we cannot focus the laser beam precisely on tumor sites without causing collateral damage to normal tissue. Considering the urgency of RB theranostic and the mentioned difficulties, the employment of subcutaneous xenograft tumor models was acceptable. However, the simplified xenograft tumor models still exhibited a deficiency that the microenvironment of orthotopic tumors could not be replaced completely by xenograft tumors, suggesting that the predictive value of data in vivo experiments was reduced to some extent. Thus, the future experiments would be performed on the more mature RB model, such as the orthotopic tumor of rabbits, to further verify the effects of FCNPIFEs.

Conclusion

In this study, FCNPIFEs were designed as folate/magnetic dual-target multifunctional nanoplatforms to integrate US/PA/MR imaging and NIR-excited synergistic PDT/PTT for RB therapy. The FCNPIFEs relieved design flaws of existing nanoplatforms, including the insufficient targeting performance, the complex synthesis with high cost, and different excitation conditions required for multiple treatments. In our study, firstly, FCNPIFEs achieved significant intratumoral accumulations through the advantage of folate/magnetic dual-target. Secondly, PFH, ICG and SPIONs were used as multifunctional components of FCNPIFEs to simultaneously realize the functions of imaging /treatment or imaging/targeting, simplifying the synthesis process to some extent and reducing the synthesis cost compared with the other such theranostics nanoparticles.[51,52] Thirdly, ICG could display remarkable photothermal and photodynamic effects under the same laser excitation. Though the PDT efficacy of ICG was limited by hypoxia in tumors due to the high oxygen dependency, PFH in FCNPIFEs showed outstanding oxygen reserve capacity and effectively alleviated intratumor hypoxia. Based on the improved PDT effect, FCNPIFEs successfully produced a synergistic PDT/PTT antitumor effect, which is contributed to the down-regulated HSP70 by the enhanced ROS generation. In addition, FCNPIFEs were also

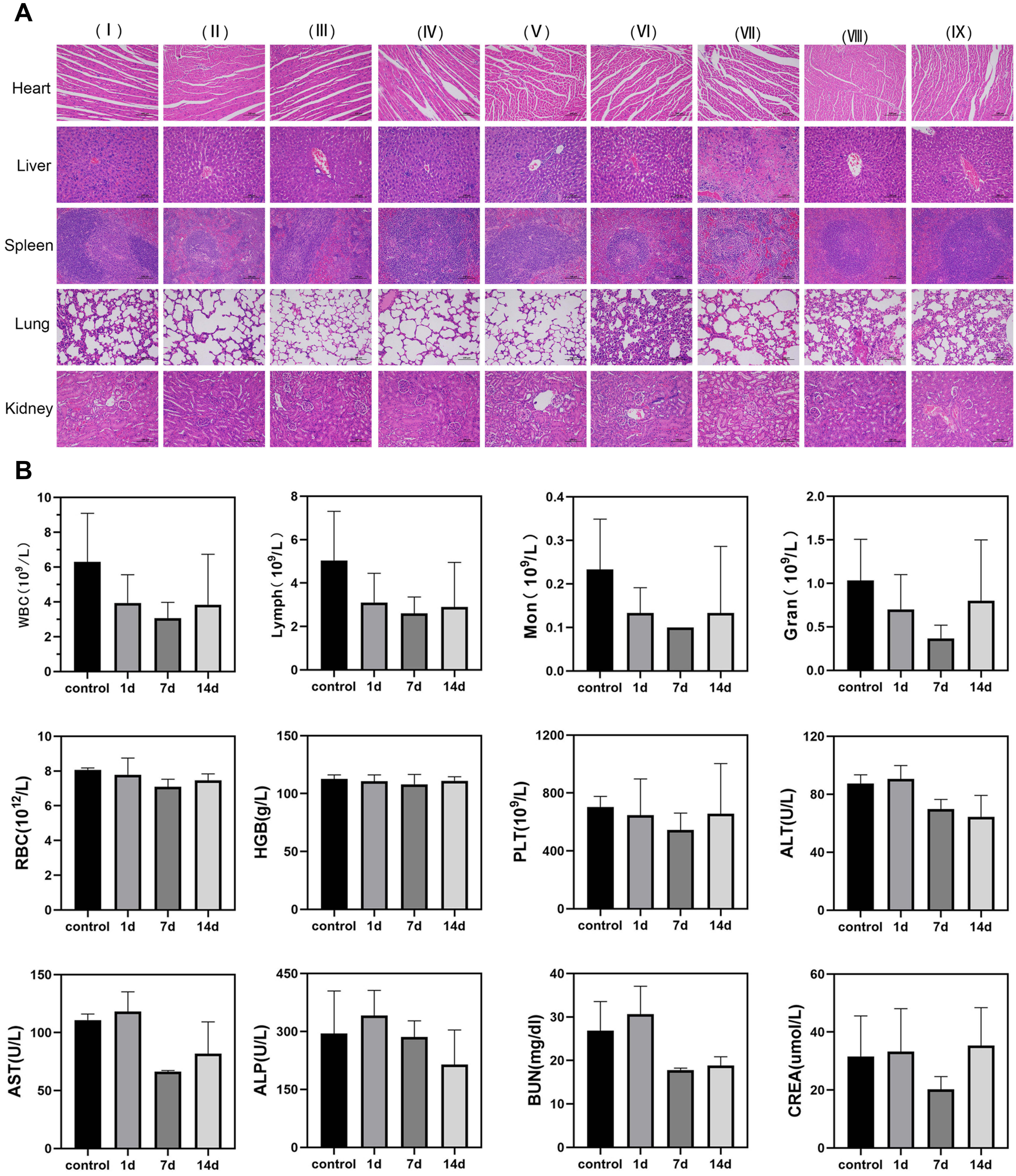

Figure 9 In vivo biosafety of FCNPIFE. (**A**) HE staining of major organs on the 3rd day after mice received different treatments. (Scale bar: 100μm). (**B**) Blood biochemical examination of mice at 0, 1, 7 and 14d after injection of FCNPIFEs.

verified to have an excellent biosafety in vitro and in vivo. The in vivo therapy results also indicated that FCNPIFEs could inhibit tumor growth to almost regression without significant systemic toxicity.

In summary, the exquisite and coordinated design of multifunctional FCNPIFEs showed a good potential in clinical application, shedding new light in promoting the early diagnosis and treatment of retinoblastoma with high biosafety.

Acknowledgments

The authors are sincerely grateful for financial support from the National Natural Science Foundation for Youth of China (No. 81901765) and the National Natural Science Foundation of China (No. 82070976). Wendi Zheng and Xing Li are co-first authors and contributed equally to this study. Xiyuan Zhou and Mingxing Wu are co-corresponding authors and contributed equally to this study.

Disclosure

The authors report no conflicts of interest in this work.

References

1. Skalet AH, Gombos DS, Gallie BL, et al. Screening children at risk for retinoblastoma. *Ophthalmology*. 2018;125(3):453–458. doi:10.1016/j.ophtha.2017.09.001
2. Moeez Uddin M, Farooque U, Aziz MZ, et al. Different types of clinical presentations and stages of retinoblastoma among children. *Cureus*. 2020. doi:10.7759/cureus.10672
3. Ancona-Lezama D, Dalvin L, Shields C. Modern treatment of retinoblastoma: a 2020 review. *Indian J Ophthalmol*. 2020;68(11):2356. doi:10.4103/ijo.IJO_721_20
4. Castela G, Providência J, Monteiro M, et al. Treatment of advanced retinoblastoma in children evacuated from low-income countries: experience from a national referral center in Portugal. *OPTH*. 2021;15:4765–4773. doi:10.2147/OPTH.S343919
5. Rössler J, Dietrich T, Pavlakovic H, et al. Higher vessel densities in retinoblastoma with local invasive growth and metastasis. *Am J Pathol*. 2004;164(2):391–394. doi:10.1016/S0002-9440(10)
6. Garbayo E, Pascual-Gil S, Rodríguez-Nogales C, Saludas L. Nanomedicine and drug delivery systems in cancer and regenerative medicine. *WIREs Nanomed Nanobiotechnol*. 2020;12(5):548. doi:10.1002/wnan.1637
7. Wang J, Song W, Wang X, et al. Tumor-self-targeted "thermoferroptosis-sensitization" magnetic nanodroplets for multimodal imaging-guided tumor-specific therapy. *Biomaterials*. 2021;277:121100. doi:10.1016/j.biomaterials.2021.121100
8. Dai Z, Wang Q, Tang J, et al. Immune-regulating bimetallic metal-organic framework nanoparticles designed for cancer immunotherapy. *Biomaterials*. 2022;280:121261. doi:10.1016/j.biomaterials.2021.121261
9. Asadi M, Beik J, Hashemian R, et al. MRI-based numerical modeling strategy for simulation and treatment planning of nanoparticle-assisted photothermal therapy. *Physica Medica*. 2019;66:124–132. doi:10.1016/j.ejmp.2019.10.002
10. Chen Y, Zhang F, Wang Q, Tong R, Lin H, Qu F. Near-infrared light-mediated LA-UCNPs@SiO 2 -C/HA@mSiO 2 -DOX@NB nanocomposite for chemotherapy/PDT/PTT and imaging. *Dalton Trans*. 2017;46(41):14293–14300. doi:10.1039/C7DT02529G
11. Kim H, Lee D. Near-infrared-responsive cancer photothermal and photodynamic therapy using gold nanoparticles. *Polymers*. 2018;10(9):961. doi:10.3390/polym10090961
12. Nagai Y, Nakamura K, Ohno J, Kawaguchi M, Fujigaya T. Antibody-conjugated gel-coated single-walled carbon nanotubes as photothermal agents. *ACS Appl Bio Mater*. 2021;4(6):5049–5056. doi:10.1021/acsabm.1c00299
13. Alamzadeh Z, Beik J, Mirrahimi M, et al. Gold nanoparticles promote a multimodal synergistic cancer therapy strategy by co-delivery of thermo-chemo-radio therapy. *Eur J Pharmaceutical Sci*. 2020;145:105235. doi:10.1016/j.ejps.2020.105235
14. Mirrahimi M, Beik J, Mirrahimi M, et al. Triple combination of heat, drug and radiation using alginate hydrogel co-loaded with gold nanoparticles and cisplatin for locally synergistic cancer therapy. *Int J Biol Macromol*. 2020;158:617–626. doi:10.1016/j.ijbiomac.2020.04.272
15. Gao G, Jiang Y, Sun W, et al. Molecular targeting-mediated mild-temperature photothermal therapy with a smart albumin-based nanodrug. *Small*. 2019;1:1900501. doi:10.1002/smll.201900501
16. Wang W, Zhang X, Ni X, et al. Semiconducting polymer nanoparticles for NIR-II fluorescence imaging-guided photothermal/thermodynamic combination therapy. *Biomater Sci*. 2022. doi:10.1039/D1BM01646F
17. Dai Y, Wang B, Sun Z, et al. Multifunctional theranostic liposomes loaded with a hypoxia-activated prodrug for cascade-activated tumor selective combination therapy. *ACS Appl Mater Interfaces*. 2019;11(43):39410–39423. doi:10.1021/acsami.9b11080
18. Teixo R, Laranjo M, Abrantes AM, et al. Retinoblastoma: might photodynamic therapy be an option? *Cancer Metastasis Rev*. 2015;34(4):563–573. doi:10.1007/s10555-014-9544-y
19. Yang J, Hou M, Sun W, et al. Sequential PDT and PTT Using Dual-Modal Single-Walled Carbon Nanohorns Synergistically Promote Systemic Immune Responses against Tumor Metastasis and Relapse. *Adv Sci*. 2020;7(16):2001088. doi:10.1002/advs.202001088
20. Zhu H, Cheng P, Chen P, Pu K. Recent progress in the development of near-infrared organic photothermal and photodynamic nanotherapeutics. *Biomater Sci*. 2018;6(4):746–765. doi:10.1039/C7BM01210A
21. Pu Y, Zhu Y, Qiao Z, et al. A Gd-doped polydopamine (PDA)-based theranostic nanoplatform as a strong MR/PA dual-modal imaging agent for PTT/PDT synergistic therapy. *J Mater Chem B*. 2021;9(7):1846–1857. doi:10.1039/D0TB02725A
22. Zhang D, Wu M, Zeng Y, et al. Chlorin e6 Conjugated Poly(dopamine) Nanospheres as PDT/PTT Dual-Modal Therapeutic Agents for Enhanced Cancer Therapy. *ACS Appl Mater Interfaces*. 2015;7(15):8176–8187. doi:10.1021/acsami.5b01027
23. Bhavane R, Starosolski Z, Stupin I, Ghaghada KB. NIR-II fluorescence imaging using indocyanine green nanoparticles. *Sci Rep*. 2018;8(1):14455. doi:10.1038/s41598-018-32754-y
24. Park T, Lee S, Amatya R, et al. ICG-Loaded PEGylated BSA-Silver Nanoparticles for Effective Photothermal Cancer Therapy. *IJN*. 2020;15:5459–5471. doi:10.2147/IJN.S255874
25. Liu J, Yin Y, Yang L, et al. Nucleus-Targeted Photosensitizer Nanoparticles for Photothermal and Photodynamic Therapy of Breast Carcinoma. *IJN*. 2021;16:1473–1485. doi:10.2147/IJN.S284518
26. Xue P, Hou M, Sun L, et al. Calcium-carbonate packaging magnetic polydopamine nanoparticles loaded with indocyanine green for near-infrared induced photothermal/photodynamic therapy. *Acta Biomaterialia*. 2018;81:242–255. doi:10.1016/j.actbio.2018.09.045

27. Liu F, Chen Y, Li Y, et al. Folate-receptor-targeted laser-activable poly(lactide-co-glycolic acid) nanoparticles loaded with paclitaxel/indocyanine green for photoacoustic/ultrasound imaging and chemo/photothermal therapy. *IJN*. 2018;13:5139–5158. doi:10.2147/IJN.S167043
28. Yu M, Xu X, Cai Y, Zou L, Shuai X. Perfluorohexane-cored nanodroplets for stimulations-responsive ultrasonography and O 2 -potentiated photodynamic therapy. *Biomaterials*. 2018;175:61–71. doi:10.1016/j.biomaterials.2018.05.019
29. Huang C, Zhang Z, Guo Q, et al. A Dual-Model Imaging Theragnostic System Based on Mesoporous Silica Nanoparticles for Enhanced Cancer Phototherapy. *Adv Healthcare Mater*. 2019;8(19):1900840. doi:10.1002/adhm.201900840
30. Qin H, Teng R, Liu Y, Li J, Yu M. Drug Release from Gelsolin-Targeted Phase-Transition Nanoparticles Triggered by Low-Intensity Focused Ultrasound. *IJN*. 2022;17:61–71. doi:10.2147/IJN.S341421
31. Sheng D, Liu T, Deng L, et al. Perfluorooctyl bromide & indocyanine green co-loaded nanoliposomes for enhanced multimodal imaging-guided phototherapy. *Biomaterials*. 2018;165:1–13. doi:10.1016/j.biomaterials.2018.02.041
32. Jansen RW, de Bloeme CM, Brisse HJ, et al. MR Imaging Features to Differentiate Retinoblastoma from Coats' Disease and Persistent Fetal Vasculature. *Cancers*. 2020;12(12):3592. doi:10.3390/cancers12123592
33. Bakhtiary Z, Saei AA, Hajipour MJ, Raoufi M, Vermesh O, Mahmoudi M. Targeted superparamagnetic iron oxide nanoparticles for early detection of cancer: possibilities and challenges. *Nanomedicine*. 2016;12(2):287–307. doi:10.1016/j.nano.2015.10.019
34. Dulińska-Litewka J, Łazarczyk A, Hałubiec P, Szafrański O, Karnas K, Karewicz A. Superparamagnetic Iron Oxide Nanoparticles—Current and Prospective Medical Applications. *Materials*. 2019;12(4):617. doi:10.3390/ma12040617
35. Movahedi MM, Mehdizadeh A, Koosha F, et al. Investigating the photo-thermo-radiosensitization effects of folate-conjugated gold nanorods on KB nasopharyngeal carcinoma cells. *Photodiagnosis Photodyn Ther*. 2018;24:324–331. doi:10.1016/j.pdpdt.2018.10.016
36. Jwala J, Vadlapatla RK, Vadlapudi AD, Boddu SHS, Pal D, Mitra AK. Differential Expression of Folate Receptor-Alpha, Sodium-Dependent Multivitamin Transporter, and Amino Acid Transporter (B $^{(0, +)}$) in Human Retinoblastoma (Y-79) and Retinal Pigment Epithelial (ARPE-19) Cell Lines. *J Ocular Pharmacol Therapeutics*. 2012;28(3):237–244. doi:10.1089/jop.2011.0155
37. Xiao Y, Cheng L. Vinorelbine cationic liposomes modified with wheat germ agglutinin for inhibiting tumor metastasis in treatment of brain glioma. *Artif Cells, Nanomed Biotechnol*. 2018;46(sup3):S524–S537. doi:10.1080/21691401.2018.1501377
38. Belhadj Slimen I, Najar T, Ghram A, Dabbebi H, Ben Mrad M, Abdrabbah M. Reactive oxygen species, heat stress and oxidative-induced mitochondrial damage. A review. *Int J Hyperthermia*. 2014;30(7):513–523. doi:10.3109/02656736.2014.971446
39. Wu M, Xiong H, Zou H, et al. A laser-activated multifunctional targeted nanoagent for imaging and gene therapy in a mouse xenograft model with retinoblastoma Y79 cells. *Acta Biomaterialia*. 2018;70:211–226. doi:10.1016/j.actbio.2018.02.006
40. Wang M, Yang Q, Li M, et al. Multifunctional Nanoparticles for Multimodal Imaging-Guided Low-Intensity Focused Ultrasound/ Immunosynergistic Retinoblastoma Therapy. *ACS Appl Mater Interfaces*. 2020;12(5):5642–5657. doi:10.1021/acsami.9b22072
41. Liu Y, Ai K, Liu J, Deng M, He Y, Dopamine-Melanin Colloidal LL. Nanospheres: an Efficient Near-Infrared Photothermal Therapeutic Agent for In Vivo Cancer Therapy. *Adv Mater*. 2013;25(9):1353–1359. doi:10.1002/adma.201204683
42. Sindhwani S, Syed AM, Ngai J, et al. The entry of nanoparticles into solid tumours. *Nat Mater*. 2020;19(5):566–575. doi:10.1038/s41563-019-0566-2
43. Zeng F, Du M, Chen Z. Nanosized Contrast Agents in Ultrasound Molecular Imaging. *Front Bioeng Biotechnol*. 2021;9:758084. doi:10.3389/fbioe.2021.758084
44. Wu M, Shu J. Multimodal Molecular Imaging: current Status and Future Directions. *Contrast Media Mol Imaging*. 2018;2018:1–12. doi:10.1155/2018/1382183
45. Lin X, He T, Tang R, et al. Biomimetic nanoprobe-augmented triple therapy with photothermal, sonodynamic and checkpoint blockade inhibits tumor growth and metastasis. *J Nanobiotechnol*. 2022;20(1):80. doi:10.1186/s12951-022-01287-y
46. Li K, Nejadnik H, Daldrup-Link HE. Next-generation superparamagnetic iron oxide nanoparticles for cancer theranostics. *Drug Discov Today*. 2017;22(9):1421–1429. doi:10.1016/j.drudis.2017.04.008
47. Kirchherr AK, Briel A, Mäder K. Stabilization of Indocyanine Green by Encapsulation within Micellar Systems. *Mol Pharmaceutics*. 2009;6(2):480–491. doi:10.1021/mp8001649
48. Yuan Y, Diao S, Ni X, et al. Peptide-based semiconducting polymer nanoparticles for osteosarcoma-targeted NIR-II fluorescence/ NIR-I photoacoustic dual-model imaging and photothermal/photodynamic therapies. *J Nanobiotechnol*. 2022;20(1):44. doi:10.1186/s12951-022-01249-4
49. Xi Y, Xie X, Peng Y, Liu P, Ding J, Zhou W. DNAzyme-adsorbed polydopamine@MnO $_2$ core–shell nanocomposites for enhanced photothermal therapy *via* the self-activated suppression of heat shock protein 70. *Nanoscale*. 2021;13(9):5125–5135. doi:10.1039/D0NR08845E
50. Chen WH, Luo GF, Lei Q, et al. Overcoming the Heat Endurance of Tumor Cells by Interfering with the Anaerobic Glycolysis Metabolism for Improved Photothermal Therapy. *ACS Nano*. 2017;11(2):1419–1431. doi:10.1021/acsnano.6b06658
51. Bui DT, Havelek R, Královec K, et al. Multimodal Contrast Agent Enabling pH Sensing Based on Organically Functionalized Gold Nanoshells with Mn-Zn Ferrite Cores. *Nanomaterials*. 2022;12(3):428. doi:10.3390/nano12030428
52. Zhang N, Wu Y, Xu W, Li Z, Wang L. Synergic fabrication of multifunctional liposomes nanocomposites for improved radiofrequency ablation combination for liver metastasis cancer therapy. *Drug Deliv*. 2022;29(1):506–518. doi:10.1080/10717544.2021.2008056